U.S. DEPARTMENT OF COMMERCE
National Bureau of Standards



*NBS Technical Note 1223*

# *Calibration of Aspirator-Type Ion Counters and Measurement of Unipolar Charge Densities*

*Misakian, McKnight, Fenimore*

*National Bureau of Standards*

The National Bureau of Standards[1] was established by an act of Congress on March 3, 1901. The Bureau's overall goal is to strengthen and advance the nation's science and technology and facilitate their effective application for public benefit. To this end, the Bureau conducts research and provides: (1) a basis for the nation's physical measurement system, (2) scientific and technological services for industry and government, (3) a technical basis for equity in trade, and (4) technical services to promote public safety. The Bureau's technical work is performed by the National Measurement Laboratory, the National Engineering Laboratory, the Institute for Computer Sciences and Technology, and the Institute for Materials Science and Engineering.

## *The National Measurement Laboratory*

Provides the national system of physical and chemical measurement; coordinates the system with measurement systems of other nations and furnishes essential services leading to accurate and uniform physical and chemical measurement throughout the Nation's scientific community, industry, and commerce; provides advisory and research services to other Government agencies; conducts physical and chemical research; develops, produces, and distributes Standard Reference Materials; and provides calibration services. The Laboratory consists of the following centers:

- Basic Standards[2]
- Radiation Research
- Chemical Physics
- Analytical Chemistry

## *The National Engineering Laboratory*

Provides technology and technical services to the public and private sectors to address national needs and to solve national problems; conducts research in engineering and applied science in support of these efforts; builds and maintains competence in the necessary disciplines required to carry out this research and technical service; develops engineering data and measurement capabilities; provides engineering measurement traceability services; develops test methods and proposes engineering standards and code changes; develops and proposes new engineering practices; and develops and improves mechanisms to transfer results of its research to the ultimate user. The Laboratory consists of the following centers:

- Applied Mathematics
- Electronics and Electrical Engineering[2]
- Manufacturing Engineering
- Building Technology
- Fire Research
- Chemical Engineering[2]

## *The Institute for Computer Sciences and Technology*

Conducts research and provides scientific and technical services to aid Federal agencies in the selection, acquisition, application, and use of computer technology to improve effectiveness and economy in Government operations in accordance with Public Law 89-306 (40 U.S.C. 759), relevant Executive Orders, and other directives; carries out this mission by managing the Federal Information Processing Standards Program, developing Federal ADP standards guidelines, and managing Federal participation in ADP voluntary standardization activities; provides scientific and technological advisory services and assistance to Federal agencies; and provides the technical foundation for computer-related policies of the Federal Government. The Institute consists of the following centers:

- Programming Science and Technology
- Computer Systems Engineering

## *The Institute for Materials Science and Engineering*

Conducts research and provides measurements, data, standards, reference materials, quantitative understanding and other technical information fundamental to the processing, structure, properties and performance of materials; addresses the scientific basis for new advanced materials technologies; plans research around cross-country scientific themes such as nondestructive evaluation and phase diagram development; oversees Bureau-wide technical programs in nuclear reactor radiation research and nondestructive evaluation; and broadly disseminates generic technical information resulting from its programs. The Institute consists of the following Divisions:

- Ceramics
- Fracture and Deformation [3]
- Polymers
- Metallurgy
- Reactor Radiation

[1] Headquarters and Laboratories at Gaithersburg, MD, unless otherwise noted; mailing address Gaithersburg, MD 20899.
[2] Some divisions within the center are located at Boulder, CO 80303.
[3] Located at Boulder, CO, with some elements at Gaithersburg, MD.

*NBS Technical Note 1223*

# *Calibration of Aspirator-Type Ion Counters and Measurement of Unipolar Charge Densities*

Martin Misakian, Ronald McKnight, Charles Fenimore

Center for Electronics and
Electrical Engineering
National Engineering Laboratory
National Bureau of Standards
Gaithersburg, MD 20899

Issued May 1986


**U.S. Department of Commerce**
Malcolm Baldrige, Secretary
National Bureau of Standards
Ernest Ambler, Director

National Bureau of Standards
Technical Note 1223
Natl. Bur. Stand. (U.S.),
Tech. Note 1223
74 pages (May 1986)
CODEN: NBTNAE

U.S. Government Printing Office
Washington: 1986

For sale by the Superintendent
of Documents,
U.S. Government Printing Office,
Washington, DC 20402

TABLE OF CONTENTS

LIST OF FIGURES

Page

## LIST OF TABLES

# Calibration of Aspirator-type Ion Counters and Measurement of Unipolar Charge Densities


## ABSTRACT

The characterization of a parallel plate apparatus which can produce a unipolar ion density that is suitable for calibrating aspirator-type ion counters operating in the ground plane is described. The influence of a dc electric field, air motion, Coulomb repulsion and diffusion on the transport of ions into the ion counter are examined to determine their effects on instrument calibration and measurements in the vicinity of high voltage dc transmission lines. An ion density which is known with an uncertainty of less than ±9% is used to check the performance of an ion counter with and without a duct at its entrance. The results of laboratory measurements of ion density under a monopolar high voltage line, which complement the studies with the parallel-plate apparatus, are also described.



Key words: Calibration; instrumentation; ion counter; ion density; measurement; transmission line; unipolar.


## 1. INTRODUCTION

During the operation of high voltage dc (HVDC) transmission lines, significant amounts of air ions are generated because of the normally present corona. Speculation regarding possible environmental effects due to the ions and associated electric field has led to increased interest in the characterization of a number of electrical parameters in the vicinity of HVDC transmission lines [1-8]. The parameters of interest include the electric field strength $\vec{E}$, the ion current density $\vec{J}$, and the unipolar ion density $\rho$. The authors have previously reported on sources of error during measurements of $\vec{E}$ using electric field mills and vibrating-plate probes [4,8], and during measurements of $\vec{J}$ using Wilson plates [6,8]. This study considers errors during the measurement of $\rho$ using aspirator-type ion counters in the presence of dc electric fields comparable in magnitude to those found near HVDC transmission lines and in bioeffects exposure systems. A major problem in determining the measurement uncertainty has been the difficulty in performing an experimental calibration of the instrumentation. This report describes an effort to develop a known unipolar ion density in a parallel plate apparatus which is suitable for calibrating aspirator-type ion counters operating in the ground plane. The influence of a dc electric field, air motion, Coulomb repulsion and diffusion on the transport of ions into the ion counter are examined to determine their effects during instrument calibration and during ion density measurements. Laboratory measurements of ion densities beneath a monopolar high voltage line are also described.

## 2. THEORY OF OPERATION OF ASPIRATOR-TYPE ION COUNTERS

A brief description of an aspirator-type ion counter is presented here with some discussion of possible mechanisms which can introduce uncertainties during a measurement. More complete accounts of the operation of ion counters are given by Israel [9] and Tammet [10]. An aspiration-type ion counter consists of a capacitor through which air is drawn. Provision is made for applying a dc voltage across the capacitor electrodes and for measuring the

ion current due to ions of one polarity reaching one of the electrodes. The applied voltage is made sufficiently large so that at a given rate of air flow, nearly all the ions impinge on the capacitor electrodes. Schematic views of cylindrical and parallel plate ion-counter designs are shown in figure 1. A cylindrical geometry was used as early as 1901 by Ebert [11]; parallel plate geometries have been used in more recent times [12].

Under ideal conditions, the measured charge density, $\rho_m$, is given by the expression [9],

$$\rho_m = I/M \quad , \tag{1}$$

where I is the measured ion current and M is the laminar volumetric flow rate of the air through the capacitor. Equation (1) is valid for ions with mobilities equal to or greater than a "critical mobility" which is given by [9]

$$k_c = M\varepsilon_o/CV \quad , \tag{2}$$

where C is the capacitance, $\varepsilon_o$ is the permittivity of free space, and V is the voltage across the capacitor. Commercial instruments are frequently configured with selectable voltages to allow operation with different critical mobilities. It is common practice to assume that all the ions are singly charged and to convert the measured charge density to an equivalent number of ions per unit volume.

Ion counter measurements can be subject to many systematic errors. For example, the parallel-plate ion counter can show significant loss of small ions if the electrode geometry is not properly designed. The polarizing plates (plates with applied voltage) must be sufficiently recessed behind the collecting plates, or fringing electric fields can precipitate ions to the enclosure walls. Measurement results demonstrating this effect are shown in figure A5 of Appendix A. A useful empirical guide is that the polarizing plates be recessed two plate spacings behind the front of the collector plates. However, the influence of fringing fields is best shown for a given instrument by measuring the ion current as a function of polarization voltage. A further discussion of ion losses due to fringing field effects is given in Appendix A.

Measurement of the volumetric flow rate, M, is straightforward if a suitable flow meter is used, but this is usually not done in commercial instruments. For these devices, the flow rate is determined by the manufacturer and is included in a given instrument calibration. If the counter is operated in a situation where there are external winds (not normally a problem during laboratory studies), then the air flow through the instrument can be affected and the stated instrument calibration may become invalid. In parallel plate systems, an additional problem arises because of the inactive region existing between the outside collecting plates and the ion counter enclosure (figure 1-b). Air flow in this region is measured as part of the volumetric air flow but does not efficiently contribute ions to the measured current. Correction for the ion losses due to the inactive regions cannot be readily made.

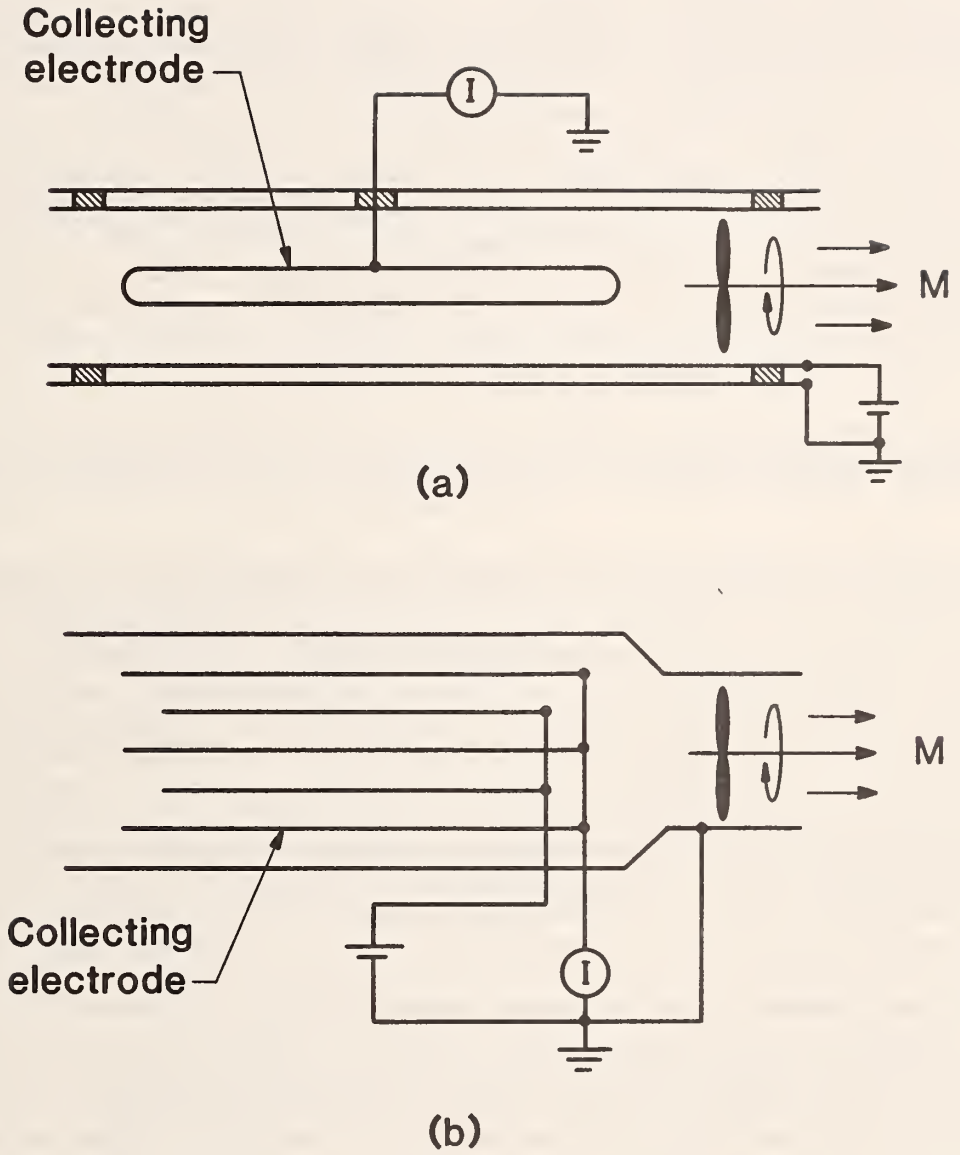


Figure 1. Schematic view of aspirator-type ion counters (a) cylindrical geometry (b) parallel plate geometry.

Vibrations of the electrodes can result in large noise signals which may obscure the actual signal if the space charge densities are small. Parallel plate counters are more susceptible to these microphonic problems than are cylindrical systems, but for all systems the effect depends on the individual construction and the magnitude of the vibration.

Polarizing potentials should be applied using a stable power source, e.g. batteries. Instabilities in the power supply will result in perturbations of the ion density measurement, since the polarizing potential is capacitively coupled to the electrometer used to measure the ion current.

In addition to the processes noted above, external dc electric fields can influence the number of ions that enter an ion counter and reach the collecting plates. Diffusion of ions may also have an effect. For the ion densities found in the vicinity of HVDC transmission lines, ion losses due to Coulomb repulsion can be a factor. The effects of an external electric field, diffusion and Coulomb repulsion on the operation of an ion counter in the ground plane are considered in detail in Section 4.

The above listing of effects which can influence an ion density measurement is not complete but demonstrates that the simple use of eq (1) can lead to significant errors.

## 3. APPARATUS FOR GENERATING KNOWN UNIPOLAR ION DENSITIES AND ELECTRIC FIELDS

As noted earlier, a factor which contributes to uncertainty in performing ion density measurements is the difficulty in generating a known ion density for experimentally calibrating the instrumentation. Because the measurements of interest involve the presence of large dc electric fields external to the ion counter, it is desirable to have an apparatus which can produce a controllable electric field as well as a known ion density. Bracken and Furumasa have reported on the use of a coaxial cylinder apparatus for testing the performance of an ion counter but do not consider in detail the uncertainties associated with the operation of the apparatus [13]. A parallel plate apparatus for producing known dc electric fields with ions has been developed at NBS for evaluation of electric field strength meters [4] and is used in the present study as a means for producing a known ion density. This section considers the unperturbed ion density in the parallel plate system and theoretical estimates of the electric field perturbation due to presence of the ion counter aperture and air motion through the aperture. The perturbation of the electric field due to an aperture is modelled with a circular aperture instead of a square aperture which is actually used during the experimental study. This approximate approach permits establishing a useful analytic relationship between the electric field and space-potential perturbations and is not expected to affect the semi-quantitative conclusions reached later. The results of measurements which help to characterize experimentally the extent of the field perturbations are described in Section 6.

### 3.1 Ion Density Profile In Parallel Plate Apparatus

Because the NBS parallel plate apparatus has been described in detail previously [4], it is discussed only briefly here. A schematic view of the

apparatus is shown in figure 2. Ions generated by stainless steel corona wires are directed both upward (to the cap) and downward to the first screen. Ions not collected on the first screen continue downward to the second screen which is the top "plate" of a parallel plate system. The ions which pass through the top plate travel a distance d to the bottom plate and form the current density J. Electrically isolated current sensing patches mounted on the bottom plate are used to measure J. The side dimensions of the parallel plates are 1.7 m x 1.7 m and the spacing is near 0.17 m for the present studies.

The solution of Poisson's equation in one dimension yields expressions for the electric field strength, E(z), and electric space potential, $\Phi(z)$, between the parallel plates [4]

$$E(z) = [E_o^2 + 2J(d-z)/K\varepsilon_o]^{1/2} \quad , \text{ and} \tag{3}$$

$$\Phi(z) = V_t - (K\varepsilon_o/3J)[(E_o^2 + 2J(d-z)/K\varepsilon_o)^{3/2} - E_o^3] \quad , \tag{4}$$

where $V_t$ is the potential of the top plate (z=d), $E_o$ is the electric field at the top plate, and K is the average mobility.

Following procedures described in Ref. [4], the values of K and $E_o$ can be determined experimentally, thus permitting the calculation of E from eq (3) for a given current density. The constitutive relation for conduction current density,

$$J = \rho K E \quad , \tag{5}$$

can then be used to determine the total charge density, $\rho$, as a function of z. It should be noted that J is approximately constant between the parallel plates because there are no sinks or sources of ions in this region. The ion density decreases and the electric field increases as a function of distance, z, from the top plate.

Figure 3 shows the results of model calculations of normalized positive ion density for $J = 1.0 \times 10^{-6}$ A/m$^2$, $K = 1.3 \times 10^{-4}$ m$^2$/Vs, $V_t = 2650$ V, and d = 0.17 m. A decrease of 49% in ion density occurs between the top and bottom plates. Reducing J by a factor of ten while keeping K, $V_t$, and d fixed results in a decrease of ion density between the plates of only 6.0%. The relatively small change in $\rho$ for the second case suggests that the parallel plate apparatus may be used for generating a "known" or calculable ion density (i.e., in this example, known within about ±3%) for calibrating an aspirator-type ion counter operating in the ground plane. However, in order to use eqs (3) and (5) to calculate the unperturbed charge density profile, it must be shown that (1) the perturbation of the electric field due to the aperture of the ion counter does not extend significantly to the upper plate of the apparatus, and (2) the influence of the air motion due to operation of the ion counter is likewise restricted mainly to the region near the aperture. Figure 4 shows schematically the conditions described above.

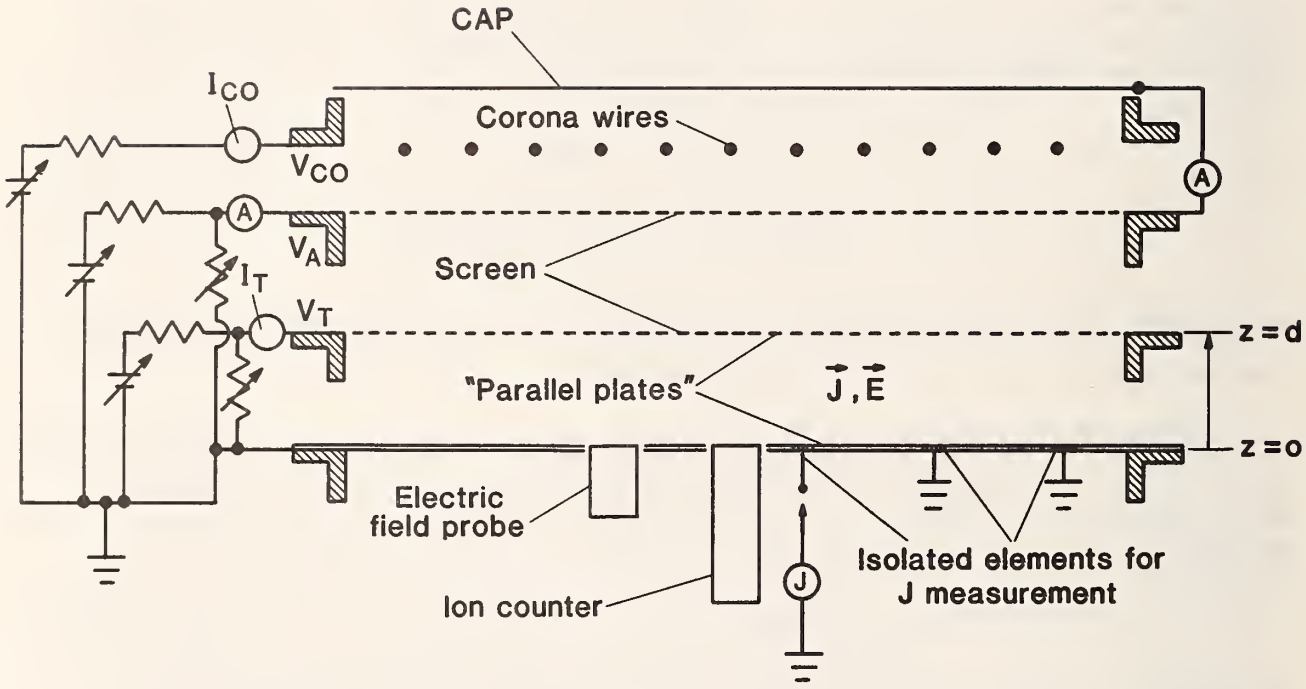


Figure 2. Schematic view of NBS parallel plate apparatus. The arrangement shown is appropriate for generating an electric field with positive space charge. The top and bottom plates of the parallel plate system are located in the planes z = d and z = 0. The corona wires are oriented parallel to one another and are perpendicular to the plane of the figure.

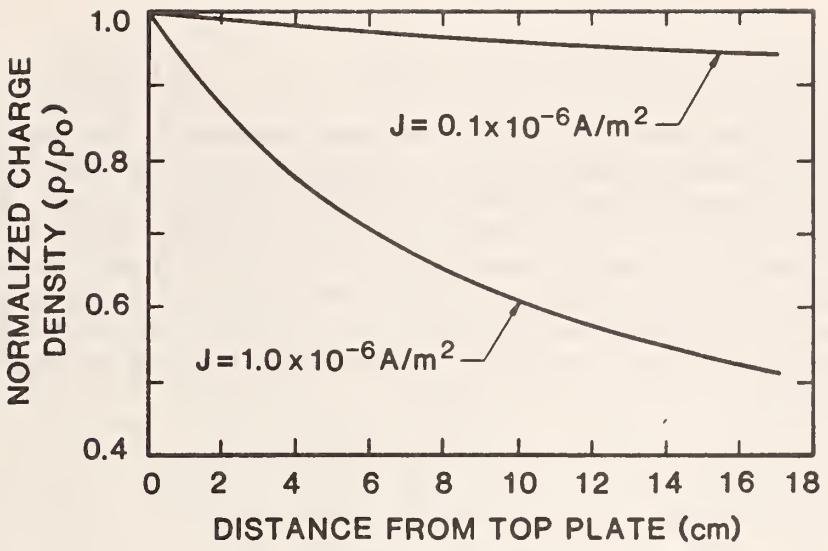


Figure 3. Normalized charge density profiles for two current densities, $1 \times 10^{-6}$ A/m$^2$ amd $0.1 \times 10^{-6}$ A/m$^2$. The calculated results assume that $V_t$ = 2650 V, K = $1.3 \times 10^{-4}$ m$^2$/Vs, and d = 0.17 m.

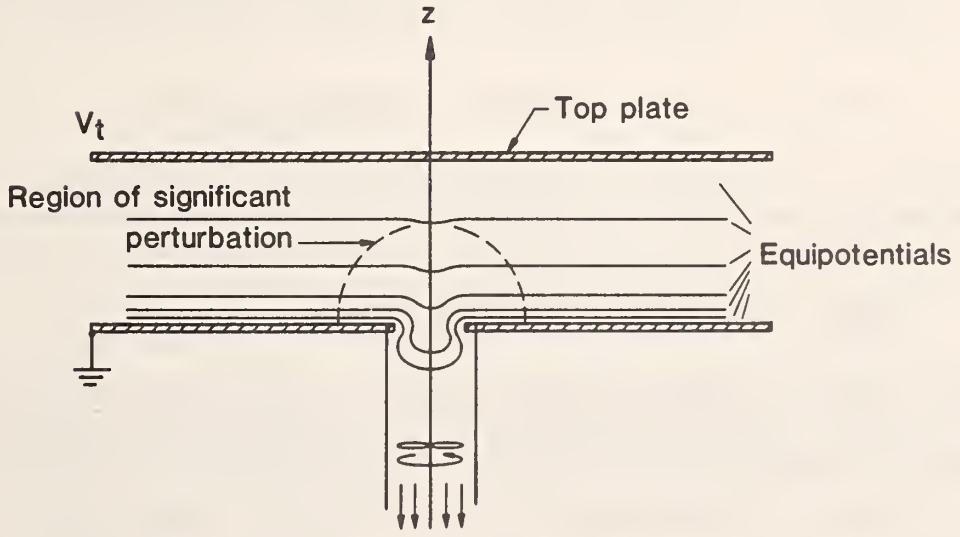


Figure 4. Schematic view showing that perturbations of electric field due to an aperture in the ground plane and air motion do not extend across the parallel plate spacing.

### 3.2 Electric Field Perturbations Due To Aperture

An estimate of the electric field perturbation due to an aperture in the ground plane can be made by numerically calculating the electric field for the geometry shown in figure 4, in the absence of space charge. Such a calculation has been performed at NBS [14], but the uncertainties in the field values and the associated space potentials are not well characterized. Analytic expressions for the electric field and potential for an aperture in the ground plane of a large parallel plate system have been derived by Fry [15]. The electric potential, $\Phi'$, and field, $E'$, along the symmetry axis (z-axis) are given by

$$\Phi' = E_u \left[z/2 + R/\pi + (z/\pi) \tan^{-1}(z/R)\right] \quad , \tag{6}$$

and

$$E' = E_u\left[(1/2) + zR/\pi(R^2 + z^2) + (1/\pi) \tan^{-1}(z/R)\right] \quad , \tag{7}$$

where $E_u$ is the unperturbed uniform electric field (prior to introduction of aperture) and R is the radius of the aperture. Expressing eqs (6) and (7) as normalized by the unperturbed potential ($E_u z$) and unperturbed uniform electric field ($E_u$), respectively, we have

$$(\Phi'/E_u z) = \left[1/2 + R/\pi z + (1/\pi)\tan^{-1}(z/R)\right] \quad , \tag{8}$$

and

$$(E'/E_u) = \left[1/2 + zR/\pi(R^2+z^2) + (1/\pi)\tan^{-1}(z/R)\right] \quad . \tag{9}$$

As z increases, the departure of $\Phi'$ and $E'$ from the corresponding uniform field values decreases and the magnitude of the electric field perturbation approaches twice the value of the space potential perturbation [16], i.e.,

$$\lim_{z\to\infty} |(E'-E_u)/E_u| = 2\,|(\Phi'-E_u z)/E_u z| \quad . \tag{10}$$

At a height of four radii above the aperture (along z-axis), the perturbation of $\Phi'$ is + 0.16% and the perturbation of $E'$ is -0.32%. At a given height, the perturbations decrease as a function of distance from the z-axis [15].

It is noted that the perturbation of the space-charge-free electric field predicted by eq (9) for an aperture will be more than that actually produced by an ion counter, which is an aperture connected to a conducting tube. However, the perturbations predicted by eq (9) are expected to be less than the actual values in an electric field with significant amounts of space charge because the aperture will not only perturb the surface charge densities on the parallel plates (space-charge free case), but also the volume charge density between the plates.

## 3.3 Influence of Air Motion

In a practical situation, the measurements could be affected by air motion due to the ion counter and by external sources such as wind, ventilating equipment, etc. The present experiment was designed to elucidate the effects of air motion produced by the ion counter, so all other sources of air motion were negligible. The perturbation of the electric field via perturbation of ion trajectories due to air motion produced by the ion counter cannot be readily calculated because the air velocity is a complicated function of position. However, knowledge of the air speed as a function of distance from the aperture does provide some insight into the problem. Several approximate theoretical treatments of air flow through an aperture can be found in textbooks. For example, Lamb [17] provides theoretical descriptions for non-viscous flow through an aperture using a two-dimensional analysis, a three-dimensional analysis in prolate spheroidal coordinates, and a three dimensional analysis assuming sinks in the plane of the aperture which increase in strength as the edge of the aperture is approached. A model calculation assuming sinks of constant strength in the plane of the aperture is developed in Appendix B and is found to be in better agreement with measurements along the central axis of an aperture (see figure B3) than any of the above models. The constant sink model predicts a velocity $\vec{u}$ given by the expression

$$\vec{u}(\vec{r}) = (-u_o/2\pi)\iint_{\Omega} |\vec{r}-\vec{r}'|^{-3}(\vec{r}-\vec{r}')dx'dy' \quad , \tag{11}$$

where $u_o$ is the air speed in the plane of the aperture, $\vec{r}$ and $\vec{r}'$ are position vectors above and in the plane of the aperture respectively, $x',y'$ are Cartesian coordinates in the plane of the aperture, and $\Omega$ is the area of the aperture. Along the central axis of a circular aperture of radius R, eq (11) reduces to

$$u = u_o[1 - z/(R^2+z^2)^{1/2}] \quad , \tag{12}$$

where the z axis is taken to be the central axis.

How well eq (11) describes the air velocity away from the z-axis is not clear. A comparison of preliminary off-axis air velocity measurements with calculated values using eq (11) indicates that near an aperture, the calculated values are too high. Air velocity measurements further from the aperture were made difficult by ambient air motion and uncertainty in the calibration of the instrumentation used for the measurements. However, an accurate expression for air velocity, while desirable, is not critical for determining several semi-quantitative results regarding the transport of ions into an ion counter.

Equation 12 indicates that at a point four radii above the aperture, the calculated air speed is 3% of $u_o$. To put this result into perspective, it should be noted that the average air speed at the entrance of a commercial ion counter can be as high as 1 m/s. This compares with a drift velocity of about 1.4 m/s for a positive ion in a 10 kV/m electric field. Thus, close to the

aperture, the air speed can be comparable to the ion drift velocity and significant perturbation of the electric field (in addition to perturbation due to the aperture) may occur. It appears that the influence of air motion caused by the fan in the ion counter at a distance of four radii above the aperture, ≈3 cm/s in the above example and of the same order of magnitude as ambient air currents, will be small.

An approximate view of how the electric field is affected by air motion can be obtained by solving Poisson's equation assuming a constant air flow parallel to the unperturbed electric field direction. Then the current density is taken to be $J = \rho(KE+W)$, where W is the air velocity, and the expressions analogous to eq (3) and (4) are found to be

$$E(z) = -(W/K) + [N^2+2J(d-z)/K\varepsilon_o]^{1/2} \quad , \text{ and} \tag{13}$$

$$\Phi(z) = V_t + (W(d-z)/K) - (K\varepsilon_o/3J)\{[N^2+2J(d-z)/K\varepsilon_o]^{3/2}-N^3\} \quad , \tag{14}$$

where $N = (W/K)+E_o$. Comparisons of E(z) calculated with $W = 0$ and $W \neq 0$ permits rough estimates of the influence of air motion. For example, for the experimental conditions in Sections 6 and 7, the change in E(z) 11.3 cm above the bottom plate is less than 0.04% when W is changed from zero to 3 cm/s. The model calculation may not be unreasonable because the air velocity rapidly decreases as a function of distance from the aperture and changes slowly at a distance of four radii above the aperture (i.e., nearly constant, see fig. B3). The "effective radius" of the aperture used during the measurements in Sections 6 and 7 is 2.8 cm. Thus, for the experimental conditions of the present study, it appears that significant perturbations of the electric field due to air motion do not extend to the top plate of the parallel plate system (d=0.17m).

## 4. ION TRAJECTORIES AND LOSSES

The transport of ions into an aspirator-type ion counter under the influence of an electric field and air motion is examined in a semi-quantitative manner in this section. The actual ion trajectories are not calculated because perturbations of an electric field with space charge by an aperture with air flowing through it are not readily characterized. In the model that is considered, it is assumed that the ions travel along trajectories determined by the addition of the ion drift velocity (product of ion mobility and electric field strength) and air velocity, and do not contribute to the magnitude or direction of the electric field which is essentially space-charge free. The trajectories are taken to be in the vertical y-z plane.

The electric field is found by taking the negative gradient of the electric potential derived by Fry for a uniform space-charge-free electric field perturbed by a circular aperture of radius R in the ground plane [15],

$$\vec{E}' = -\nabla\Phi' \quad , \tag{15}$$

where

$$\Phi' = A\{\sinh\lambda + (2/\pi)[1 + \sinh\lambda \cdot \tan^{-1}(\sinh\lambda)]\}\sin\mu \quad , \tag{16}$$

$\lambda$ and $\mu$ are oblate spheroidal coordinates and are related to Cartesian coordinates by the equations

$$y = R\cosh\lambda\cos\mu \tag{17}$$

$$z = R\sinh\lambda\sin\mu \quad , \tag{18}$$

and A is $E_u R/2$. A circular aperture is used to approximate the square aperture of the ion counter that is used during the measurements described in Sections 6 and 7, but this approximation should not significantly affect the conclusions reached here.

The horizontal and vertical drift velocities, $v_y$ and $v_z$, are given by

$$v_y = KE'_y \quad , \text{ and} \tag{19}$$

$$v_z = KE'_z \quad , \tag{20}$$

where

$$E'_y = -(AS\sin\mu\cos\mu\sinh\lambda/B) + (AT\sin\mu\cos\mu\cosh\lambda/B) \quad ,$$

$$E'_z = -(AS\sin^2\mu\cosh\lambda/B) - (AT\cos^2\mu\sinh\lambda/B) \quad ,$$

$$S = [\cosh\lambda + (2/\pi)\cosh\lambda\tan^{-1}(\sinh\lambda) + (2/\pi)\tanh\lambda] \quad ,$$

$$T = [\sinh\lambda + (2/\pi) + (2/\pi)\sinh\lambda\tan^{-1}(\sinh\lambda)] \quad ,$$

and

$$B = R(\cosh^2\lambda - \cos^2\mu) \quad .$$

Useful expressions relating the hyperbolic and trigonometric functions to Cartesian coordinates in the y-z plane are [15]

$$2R^2\sinh^2\lambda = y^2+z^2-R^2+[(y^2+z^2-R^2)^2+4R^2z^2]^{1/2} \quad , \tag{21}$$

$$2R^2\cosh^2\lambda = y^2+z^2+R^2+[(y^2+z^2-R^2)^2+4R^2z^2]^{1/2} \quad , \tag{22}$$

$$2b^2\sin^2\mu = R^2-y^2-z^2+[(y^2+z^2-R^2)^2+4R^2z^2]^{1/2} \quad , \text{ and} \tag{23}$$

$$2b^2\cos^2\mu = y^2+z^2+R^2-[(y^2+z^2-R^2)^2+4R^2z^2]^{1/2} \quad . \tag{24}$$

For negative values of z, the negative root must be used in eq (21) when solving for $\sinh\lambda$.

Equation 11 is used to obtain the air velocity components above the aperture. As noted earlier, the air velocity values along the z-axis are well predicted by eq (11) but the off-axis values appear to be too high. However, the off-axis inaccuracies should not affect the conclusions of this section.

For a square aperture of side dimension 2R, eq (11) can be integrated to give the following expressions for the horizontal and vertical velocity components, $u_y$ and $u_z$:

$$u_y = -(u_o/2\pi)\log[(R+F)(-R+G)/(-R+F)(R+G)] \quad , \text{ and} \tag{25}$$

$$u_z = -(u_o/2\pi)[\tan^{-1}(R(y+R)/zG) - \tan^{-1}(R(y-R)/zF)] \quad , \tag{26}$$

where $F = [R^2+(y-R)^2+z^2]^{1/2}$ , and

$G = [R^2+(y+R)^2+z^2]^{1/2}$ .

In the y-z plane where the ion trajectories are calculated, the edge of the square aperture coincides with that of the circular aperture assumed for the drift velocity equations.

The equations of motion for positive ions under the influence of the electric field and air motion through the aperture are for z>0

$$dy/dt = v_y + u_y \quad , \text{ and} \tag{27}$$

$$dz/dt = v_z + u_z \quad , \tag{28}$$

where the ion drift and air velocities are given by eqs (19)-(20) and eqs (25)-(26). Below the plane of the aperture, the air speed is approximated by a constant velocity, $u_o$, parallel to the z-axis. The steps for obtaining eqs (19),(20),(25) and (26) are outlined in Appendix C.

Equations (27) and (28) have been solved on a computer using a variable step-variable integration method with software developed at NBS [18]. Examples of trajectories for $E_u$ = 15 kV/m, $u_o$ = 1 m/s, R = 0.025 m, and $K = 1.3 \times 10^{-4}$ $m^2/Vs$ are shown with solid lines in figure 5. The time-of-flight to the plane of the aperture for each trajectory was arbitrarily taken to be $50 \times 10^{-3}$ s. Also shown in figure 5, with dashed lines, are ion trajectories assuming no electric field; the time-of-flight is again $50 \times 10^{-3}$ s. The surfaces that bound the trajectories with and without an electric field define volumes of charge that reach the aperture during the assumed time interval. Ignoring possible loss mechanisms in and below the

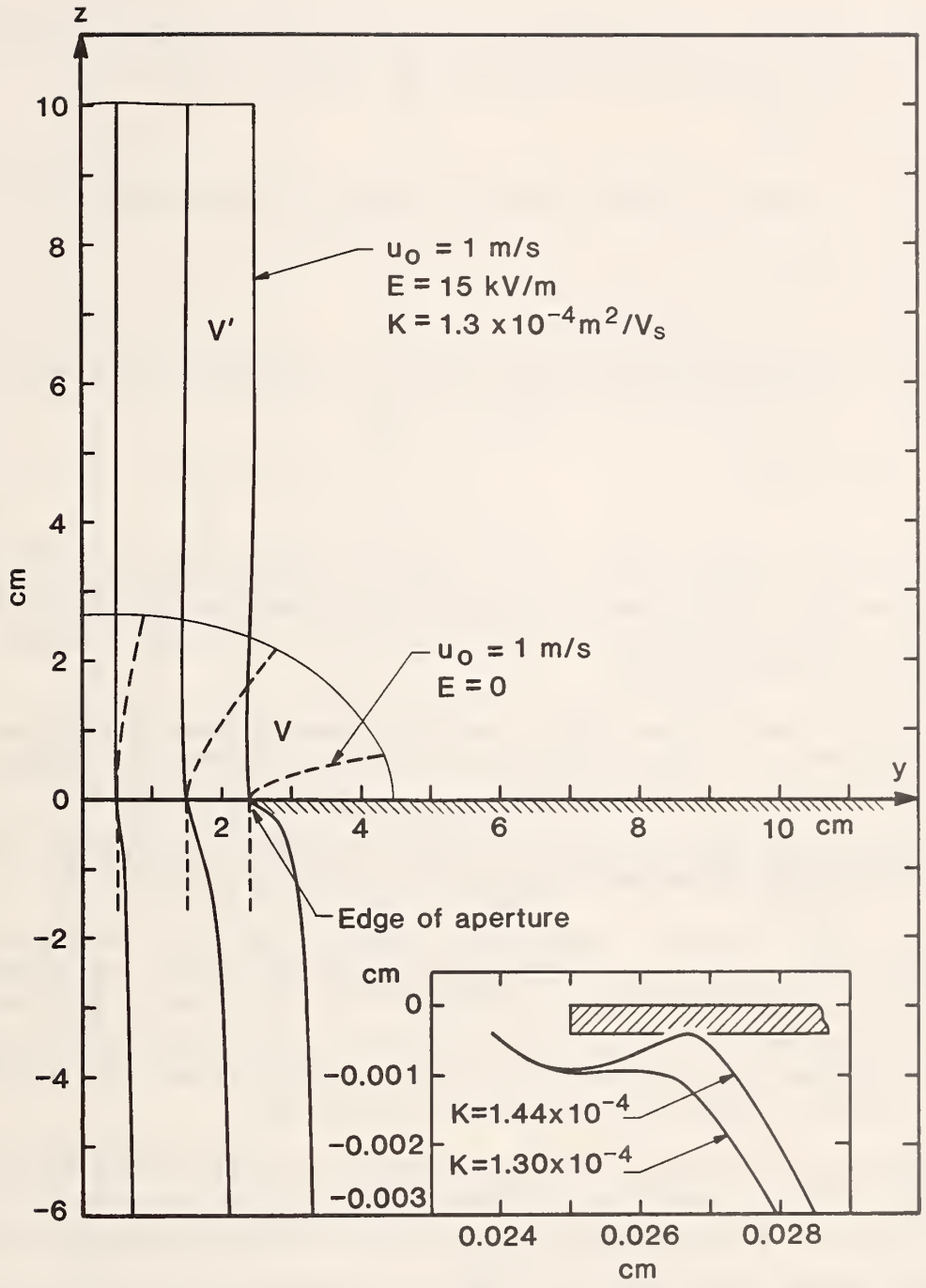


Figure 5. Ion trajectories for air speed in plane of aperture of 1 m/s. The solid curves show influence of 15 kV/m electric field. Dashed curves are for no electric field. The time-of-flight for all trajectories is 50 ms. The volume occupied by the ions that enter the aperture when E ≠ 0, V', exceeds volume of air, V, which enters in the same time. Inset shows effect of mobility value on trajectory near aperture.

plane of the aperture, the significance of the different volumes can be seen by examining the expression for measured ion density, eq (1),

$$\rho_m = I/M \quad . \tag{29}$$

Expressing I as charge per unit time, Q/t, and M as air volume per unit time, V/t,

$$\rho_m = Q/V \quad . \tag{30}$$

The charge Q can be expressed as the product of average charge density, $\rho_a$, and volume, V', occupied by the charge. Then

$$\rho_m = \rho_a V'/V \quad . \tag{31}$$

When there is no electric field, the volume of charge that enters the aperture coincides with the volume of air (V' = V) and the measured charge density equals the average charge density in space. With an electric field, V' is greater than V and the measured charge density will exceed the average value in space and thus be in error.

As the air speed is increased, the difference between V' and V decreases and $\rho_m$ approaches $\rho_a$. Figure 6 shows ion trajectories with and without an electric field for $u_o$ equal to 6 m/s. While the air speed may be unrealistically high for typical ion counter operation, the smaller difference between V' and V is apparent.

Losses in and below the plane of the aperture can occur because of ion trajectories which terminate near the edge of the aperture. For example, the inset in figure 5 suggests that some trajectories less than ≈1 mm from the edge of the aperture ($K = 1.3 \times 10^{-4}$ $m^2/Vs$) will not "clear" the aperture. This would represent approximately 8% of the ions that reach the aperture assuming a uniform charge density across the aperture.

It should also be noted that the trajectory calculations in figure 5 (except for the inset) have been performed for a single ion mobility value, $1.3 \times 10^{-4}$ $m^2/Vs$. A distribution of mobilities normally exists and ions with mobilities greater than $1.3 \times 10^{-4}$ $m^2/Vs$ could also fail to clear the aperture as shown in the inset of figure 5. Interestingly, if the product of mobility and electric field (drift velocity) is kept constant, the trajectory remains unchanged for a given air speed.

If a duct of the same cross section as the aperture is introduced below the aperture, loss of ions will occur via collisions with the wall of the duct. Assuming for simplicity that the trajectories in figure 5 remain unaffected by the duct, calculations show that ions entering the aperture 5 mm from the edge (y = 2 cm) will collide with the duct about 1.3 cm below the plane of the aperture. This loss as well as the loss of other ions passing through the aperture further from the z-axis would amount to about 36% of the

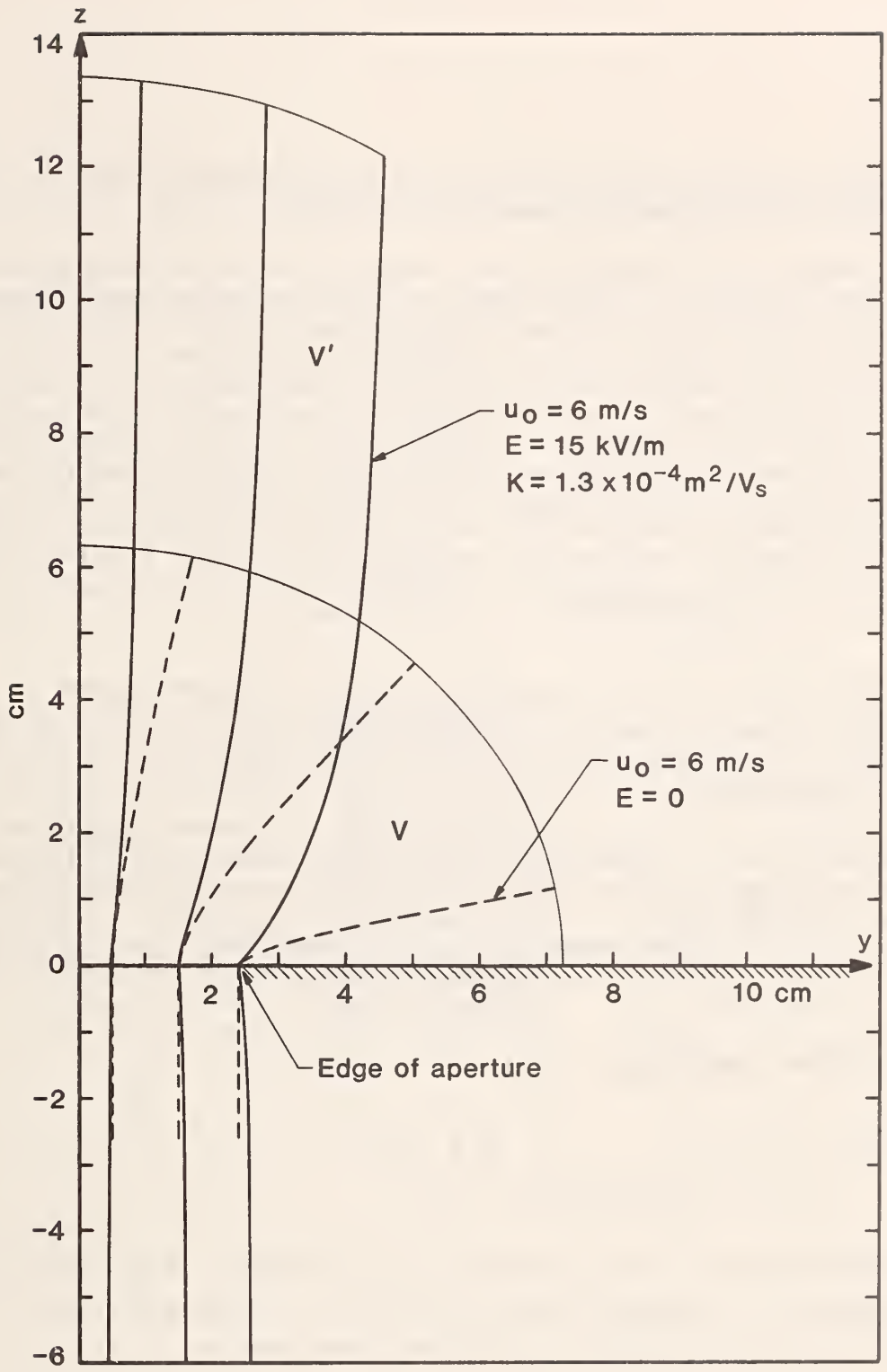


Figure 6. Ion trajectories for air speed of 6 m/s in plane of aperture. The solid curves show influence of 15 kV/m electric field. Dashed curves are for no electric field. The time-of-flight for all trajectories is 50 ms. The volume occupied by the ions that enter aperture when E ≠ 0, V', exceeds volume of air, V, which enters in same time.

total number of ions reaching the aperture, again assuming that the ion density were uniform over the area of the aperture.

The excess ions entering an ion counter due to an external electric field which attracts ions to the ion counter and the ion losses which subsequently occur to the walls of the ion counter was noted by Swann early in this century [19]. He concluded that the ion current to the walls was just equal to the excess ion current due to the electric field, independent of air speed, and that the electric field did not influence the ion density measurement [20]. However, because Swann appears to assume that all of the electric field lines terminate on the walls of the ion counter, his conclusion that all the excess ion current goes to the walls must be qualified. Some field lines could terminate on the electrodes of the ion counter and contribute to a higher ion density measurement. For example, calculations show that field lines within a radius of 5 mm of the center of the aperture will travel at least 4.5 cm below the plane of the aperture before reaching an imaginary wall at a radius of 2.5 cm.

An ion loss mechanism which has been ignored above, because of the simplifying assumption that the ion contribution to the electric field is negligible, is one which considers Coulomb repulsion between the ions. In reality charge densities in the vicinity of dc transmission lines can exceed $1 \times 10^{-8}$ C/m$^3$ [1] and the Coulomb interactions are not insignificant. The loss mechanism can be approximately modelled by considering a circular cylinder of charge initially of density $\rho(z=0)$ extending downward from the aperture along the z-axis as shown schematically in figure 7. Ignoring the electric field which penetrates the aperture from above, ions at the outer surface of the cylinder will experience a radially outward electric field given by, from Gauss' law,

$$E = \rho(z=0)R/2\varepsilon_o \quad , \tag{32}$$

and a drift velocity of

$$v_d = KE = K\rho(z=0)R/2\varepsilon_o \quad . \tag{33}$$

Under the influence of the air velocity $u_o$ along the z-axis, the ions will travel downward a distance L after a time $L/u_o$. In the same time, the radially outward displacement, s, will be approximately

$$s \approx v_d L/u_o = K\rho(z=0)RL/2\varepsilon_o u_o \quad . \tag{34}$$

If there is a cylindrical duct of radius R below the aperture, the radially displaced ions will be lost to the duct. The fraction of ions lost can be estimated by comparing ion densities in disks of thickness $\Delta z$ near the aperture and at a distance L below the aperture. The ratio of the densities is given by

$$\rho(z=L)/\rho(z=0) = \pi R^2 \Delta z/\pi(R+s)^2 \Delta z = R^2/(R+s)^2 \quad . \tag{35}$$

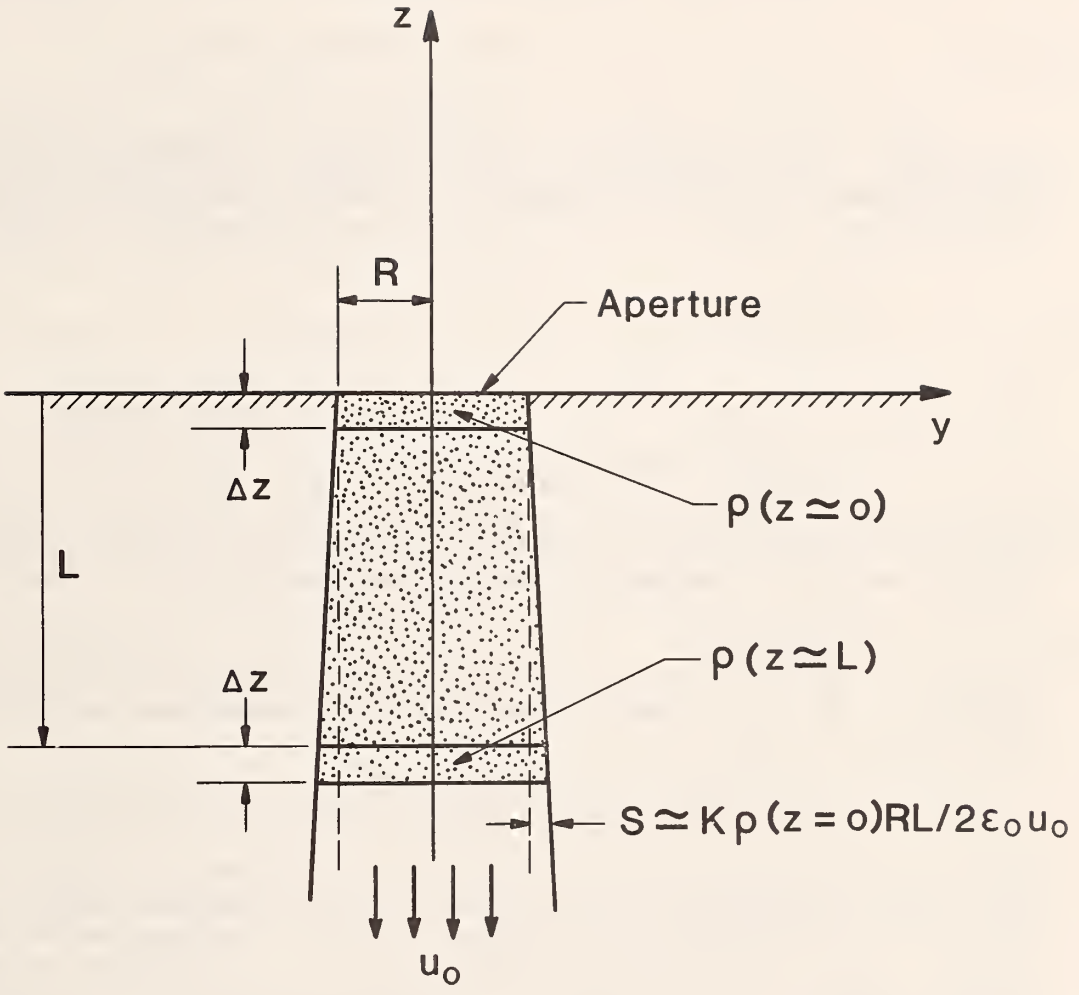


Figure 7. Schematic view showing influence of Coulomb repulsion on ions below plane of aperture. The effects of the electric field above the aperture are ignored.

The results using this expression are in good agreement with more exact treatments of the problem which are independent of geometry. For example, it can be shown that [21]

$$\rho(z_2)/\rho(z_1) = [1+(\rho(z_1)K\tau/\varepsilon_o)]^{-1} \quad , \tag{36}$$

where $\tau$ is the time-of-flight between points $z_1$ and $z_2$.

Loss of ions to the duct by diffusion represents yet another loss mechanism. For a cylindrical cloud of charge, the average square of the displacement in the radial direction because of diffusion is given by [22]

$$\overline{r^2} = 4D\tau \quad ,$$

or

$$s' \equiv \left[\overline{r^2}\right]^{1/2} = [4D\tau]^{1/2} \quad , \tag{37}$$

where D is the diffusion coefficient. Equation (37) can be rewritten in terms of the ion mobility using the Einstein equation [22]

$$K = eD/kT \quad , \tag{38}$$

where e is the ionic charge, k is the Boltzmann constant and T is the temperature in degrees Kelvin. That is

$$s' = [4kTK\tau/e]^{1/2} = [4kTKL/u_o e]^{1/2} \quad . \tag{39}$$

The lateral displacement of the ions due to the combined effects of Coulomb repulsion and diffusion as a circular cylinder of charge moves below the aperture can be estimated by adding s and s'. The relative importance of Coulomb repulsion and diffusion is found by examining the ratio of s and s'. That is,

$$s/s' = (\rho(z=0)R/4\varepsilon_o)(K\tau e/u_o kT)^{0.5} \quad . \tag{40}$$

For the experimental conditions in Section 7, s/s' is of the order of unity in a 5 cm long duct.

## 5. CALCULATED CHARGE DENSITY

In Section 3.1 it was shown that for sufficiently small ion current densities, the uncertainty in the value of the charge density between parallel plates could be made relatively small, i.e., ±3% for the example considered. Here it is shown that the charge density which the ion counter should measure

in the parallel plate system can be determined with an uncertainty less than one-half the range of values given by $\rho(z)$.

In the presence of a dc electric field, the ion current through the plane of the aperture of the ion counter is given by

$$I = \int_S \rho(x,y,0)(\vec{u}+\vec{v})\cdot d\vec{S} \tag{41}$$

where $d\vec{S}$ is an element of area in the plane of the aperture of area S, $\vec{u}$ is the air velocity and $\vec{v}$ is the ion drift velocity. If all of the ion current were to reach the collecting electrodes of the ion counter, the measured charge density obtained using eq (1) would be

$$\rho_m = I/M = \int_S \rho(x,y,0)\vec{u}\cdot d\vec{S}/\int_S \vec{u}\cdot d\vec{S} + \int_S \rho(x,y,0)\vec{v}\cdot d\vec{S}/\int_S \vec{u}\cdot d\vec{S} \quad . \tag{42}$$

The second term in eq (42) is considered an error to the measurement [19] because the validity of eq (1) rests on the assumption that the ions are transported into the ion counter only by the air that flows through the ion counter [10]. As noted earlier, it is expected that the contribution of the second term can be made negligible provided there is adequate shielding of the electric field. Thus, the charge density which should be measured in the absence of electric field effects (and ion losses below the plane of the aperture) is given by the first term of eq (42). If the first term in eq (42) can be calculated from theory, it can serve as the known value of charge density which is used to calibrate ion counters.

Lack of knowledge of the charge density in the plane of the aperture, because of perturbations, prevents the evaluation of the first term in eq (42). However, the integrals can be determined on a surface for which the perturbations of the charge density become negligibly small. This surface coincides with the surface on which the electric field perturbations become negligible and is designated $S_o$.

The shape of $S_o$ can be estimated at low air speeds by examining the spatial dependence of the electric field perturbation due to an aperture in the absence of space charge. An examination of the ratio $E'/E_u$ in the y-z plane (see eqs (19) and (20)) shows that surfaces of nearly equal perturbation (absolute value) are, because of axial symmetry, hemi-ellipsoids. The intersection of the surface with the y-z plane yields a hemi-ellipse with semi-minor and semi-major axes $y_o$ and $z_o$ as shown in figure 8. Thus, the calculated charge density can be expressed as

$$\rho_c = \int_{S_o} \rho(z)\vec{u}\cdot d\vec{S}/\int_{S_o} \vec{u}\cdot d\vec{S} = (J/K) \int_{S_o} \rho'(z)\vec{u}\cdot d\vec{S}/\int_{S_o} \vec{u}\cdot d\vec{S} \tag{43}$$

where

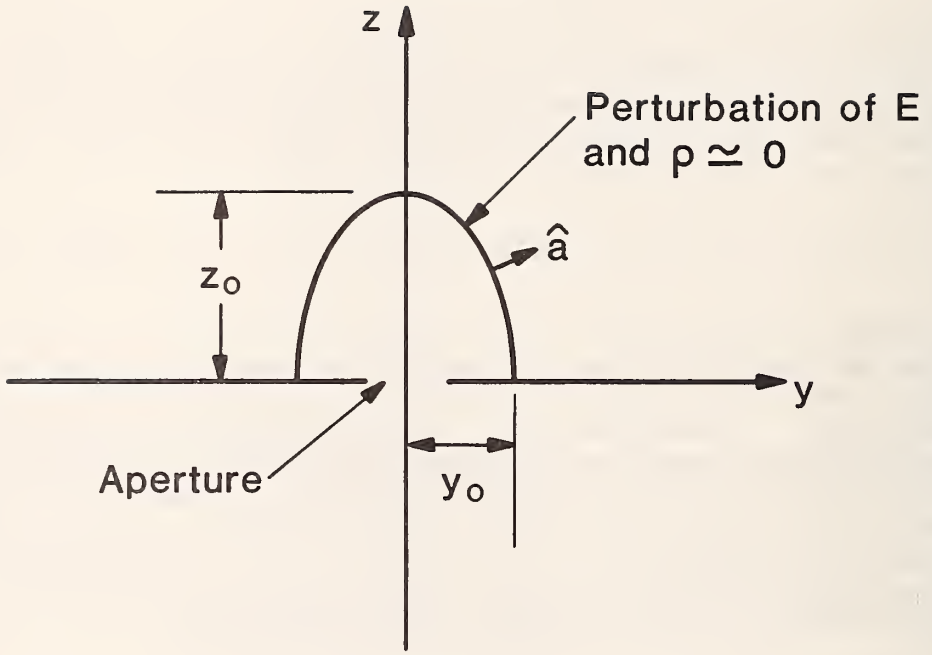


Figure 8. Hemi-ellipse and coordinates for calculating charge density, $\rho_c$.

$$d\vec{S} = \hat{a}(y,z)(2\pi y_o/z_o^2)[z_o^2(z_o^2-z^2) + y_o^2z^2]^{1/2}dz \quad ,$$

$$\hat{a}(y,z) = [(2y/y_o^2)\hat{j} + (2z/z_o^2)\hat{k}]/[(2y/y_o^2)^2 + (2z/z_o^2)^2]^{1/2} \quad ,$$

$$\vec{u} = u_y\hat{j} + u_z\hat{k} \quad ,$$

and $$\rho(z) = (J/K)\rho'(z) = J/K[E_o^2+2J(d-z)/K\varepsilon_o]^{1/2} \quad .$$

The vector $\hat{a}(y,z)$ is a unit vector normal to the hemi-ellipse in the y-z plane; $\hat{j}$ and $\hat{k}$ are unit vectors parallel to the y and z axes respectively. The uncertainty in the value of $\rho_c$ is dependent, in part, on how well $y_o$, $z_o$ and the distribution of relative air velocities on $S_o$ are known [23]. The distribution of relative air velocities on the surface of integration is the relevant parameter because $u_o$ can be factored out of the integrals in the numerator and denominator of eq (43).

## 6. MEASUREMENT RESULTS: PERTURBATION OF ELECTRIC FIELD

From the preceeding sections it is recalled that in order to calculate the ion density in the parallel plate apparatus, it must be demonstrated that the perturbation of the electric field due to the aperture of the ion counter does not significantly extend to the top plate. A similar restriction applies to the influence of air motion due to air being drawn through the ion counter. The approximate theory presented earlier on electric field perturbations due to an aperture and air flow through an aperture suggests that a parallel plate apparatus with spacing greater than four times the radius of the ion counter aperture may be adequate for producing a known ion density. In the following sections, measurements of the perturbed electric space potential in the parallel plate system as a function of distance above an aperture in the bottom plate are described and compared with space potential values without an aperture. The measurements are performed with the presence of space charge. An estimate of the electric field perturbation is then made using eq (10). The effect of air flow through the aperture on the space potential is also examined.

### 6.1 Space Potential Probe

Measurements of the electric space potential between the parallel plates, in the presence of space charge, were made with a space potential probe very similar in design to one reported by Penney and Matick [24] and Matick [25]. A sketch of the probe with its nominal dimensions is shown in figure 9. The operation of the probe is described briefly here; a full account is given in [24] and [25]. The space potential probe is supported between the parallel plates approximately along an equipotential surface (i.e., horizontally) with a copper-tube handle. The copper handle and frame support brass guard cylinders which contain the 0.0066 cm diameter stainless steel wire probe.

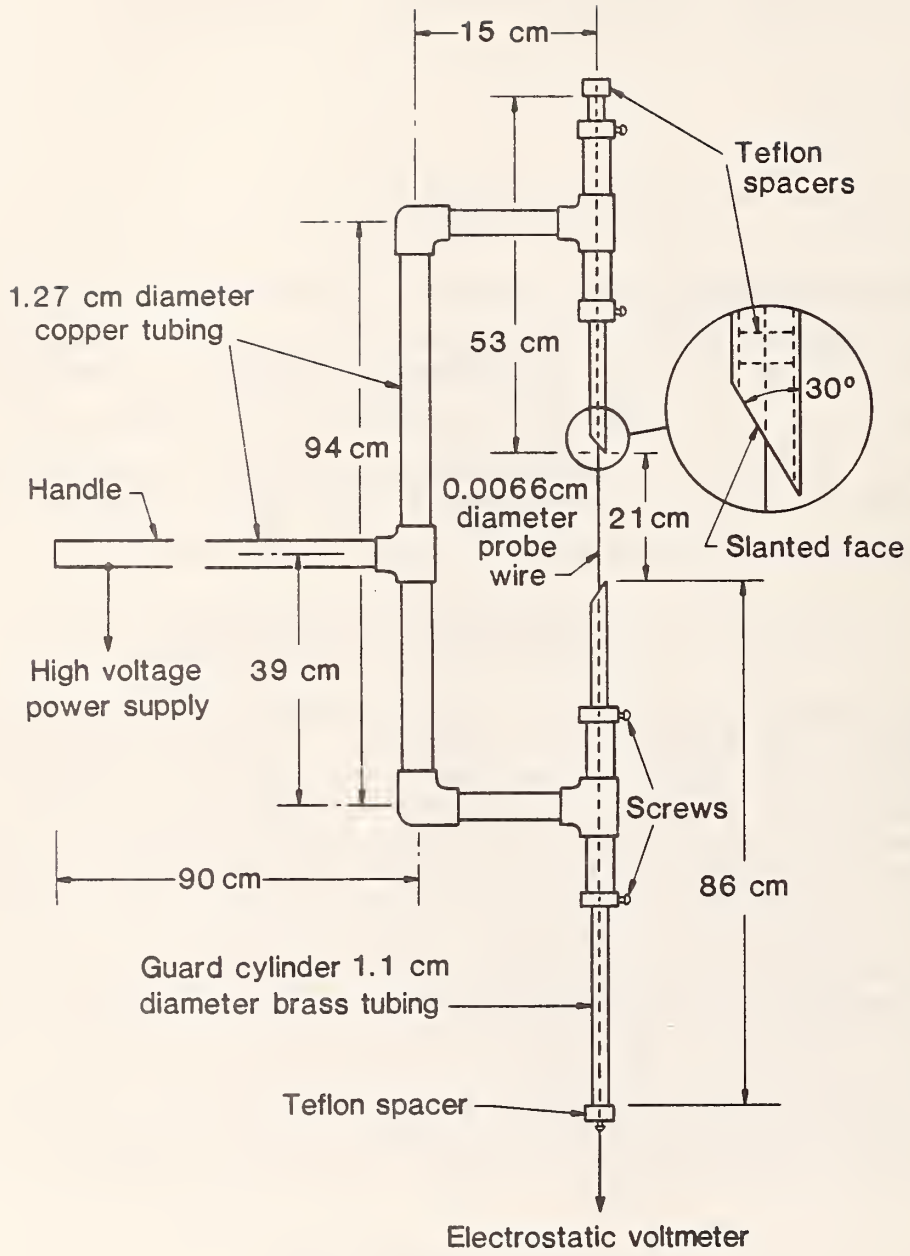


Figure 9. Schematic view of space potential probe after Penney and Matick [24,25].

The slanted ends of the guard cylinders are oriented to face the bottom grounded plate. By varying the voltage on the guard cylinders, $V_g$, and measuring the potential on the wire probe, $V_p$. with an electrostatic voltmeter, Penney and Matick report that a graph of wire potential versus guard-cylinder potential shows a plateau in the value of $V_p$ when the guard potential is near and at the space potential. The voltage of the plateau is the largest space potential intercepted by the wire probe plus a small additional potential due to charging of the wire.

The NBS potential measurement data do not show the well defined plateau reported by Penney and Matick, but do indicate relative space potentials with sufficient sensitivity for performing perturbation measurements. For example, figure 10 shows plots of probe-wire potential versus guard-cylinder potential at heights of 8.5 cm and 9.5 cm above the bottom plate of the parallel plate system. The difference in space potential for the two positions is determined by examining the intersection of the experimental curves with the line given by $V_p=V_g$. Calculation of the difference in space potential for the two heights is performed using eq (4) for the measured values of $J(1.14 \times 10^{-6}\ A/m^2)$, $V_t(1800\ V)$, $K(1.34 \times 10^{-4}\ m^2/Vs)$, and $d(0.15\ m)$, and amounts to 112 V [4]. The (vertical) difference in the measured potentials at the points of intersection with the line $V_g=V_p$ is about 109 V which is in good agreement with the calculated value. The results in figure 10 show that a difference in potential of about 9% (the change from 8.5 cm to 9.5 cm) is readily seen with this measurement technique and that potential differences of less than 1% can also be resolved. The absence of a well defined plateau may be due to insufficient isolation of the wire probe from ground because, at a given height, the value of the measured potential (point of intersection) is consistently lower than the calculated space potential.

### 6.2 Space Potential Perturbation Measurements

The calculated vertical ion density profiles in figure 3 indicate that an ion density that varies by 6% between the parallel plates can be generated when $V_t$=2650 V, $J=0.1 \times 10^{-6}\ A/m^2$, and d=0.17 m. Measurements of the current density profile on the bottom plate of the parallel plate system using a flat moveable probe reveal, for the above conditions, variations of the current density as large as ±9% near the center of the plate and temporal fluctuations of about ±3%. By increasing J to near $0.25 \times 10^{-6}\ A/m^2$ (while maintaining $V_t$ and d fixed) and increasing the drift region between the first screen and top plate from 8 cm [4] to 12 cm, the nonuniformity in J can be decreased. Figure 11 shows measurements of the current density on the bottom plate as well as the locations of a 5 cm x 5 cm aperture for an ion counter, an electrically isolated patch for measuring current (to determine J), and an electric fieldmeter probe (field mill). Each value of current density is the average of 10 measurements which in turn are time average measurements lasting 1.7 seconds. The standard deviation of the 10 measurements is typically less than 2%. Each current density value in figure 11 has been normalized by the average of 17 measurements in a circular area of 0.7 m diameter. Ignoring the

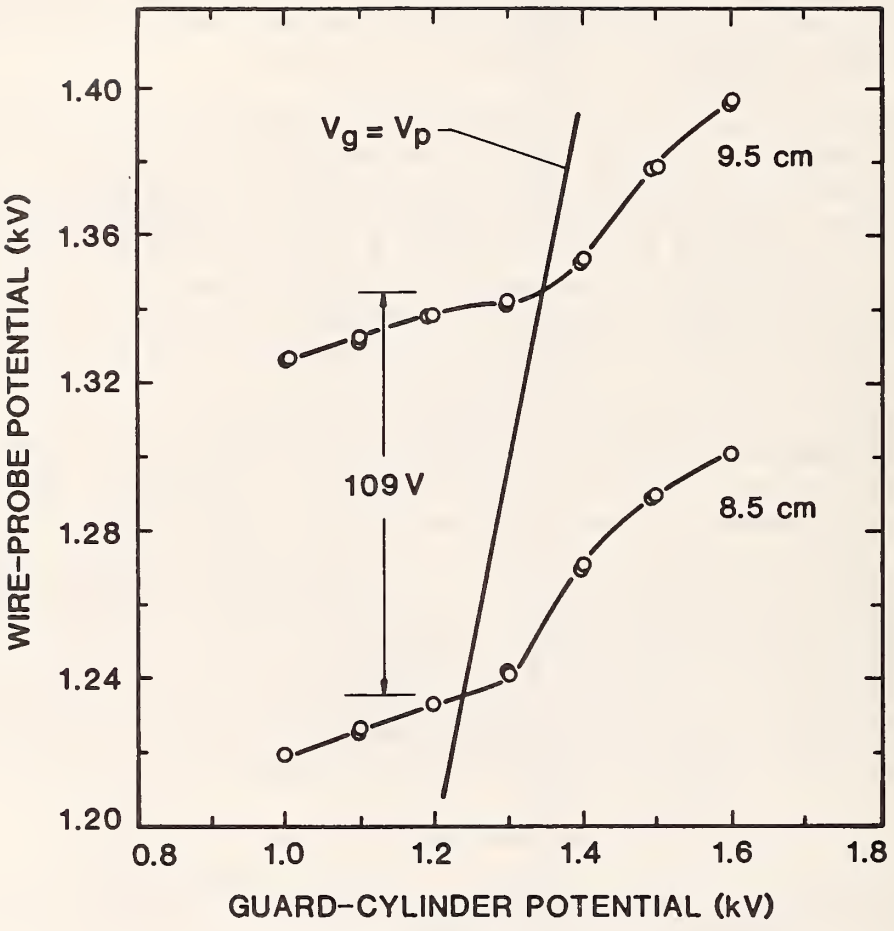


Figure 10. Measurements of space potential at 9.5 cm and 8.5 cm above the bottom plate of parallel plate system for conditions described in text. The measured potential difference agrees well with the calculated value of 112 V.

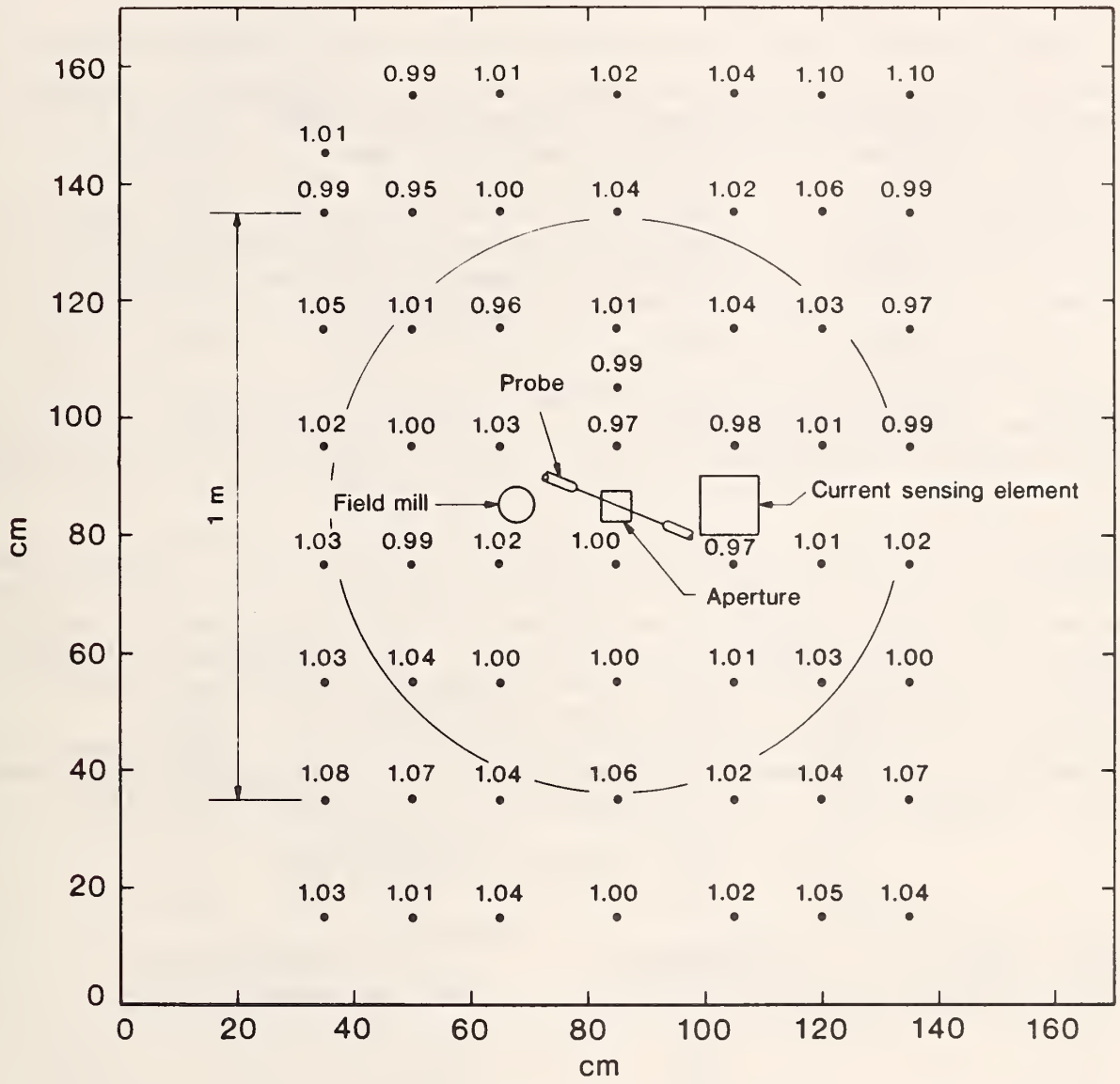


Figure 11. Measurements of the current density on the surface of the bottom plate. The measurements are obtained with a moveable probe and normalized with respect to the average of 17 measurements in a circular area of 0.7 $m_2$ diameter. The average unormalized J value is near $0.25 \times 10^{-6} A/m^2$.

temporal fluctuations, most of the current density values in a circular area of 1 m diameter are within 4% of the central average.

With $V_t$=2650 V, d=0.17, J=0.25 x $10^{-6}$ A/$m^2$, and the current density profile shown in figure 11, measurements of the space potential were made as a function of height above the bottom plate with and without a 5 cm x 5 cm aperture. The space potential probe was located over the aperture (see fig. 11) and could be moved vertically with a screw-driven vertical displacement apparatus located outside the parallel plate system. The "no-aperture" condition was established by sliding a sheet of stretched aluminum foil over the aperture. Figure 12 shows examples of graphs of probe potential, $V_p$, versus guard potential, $V_g$, near the intersections with the line $V_p=V_g$ at various heights above the bottom plate with and without the aperture. The perturbation of the space potential due to the aperture are expressed in volts and percentages at each height. For purposes of comparison with perturbations predicted by eq (8), which is valid only for space-charge free conditions, the "radius" of the square aperture is made to satisfy the relation $\pi R^2$=25 $cm^2$, i.e., R=2.82 cm. Table 1 shows the results of perturbation measurements made over a period of several days. Uncertainties in the perturbation measurements are shown in parentheses in Table 1 and are due mainly to uncertainties in reading the electrostatic voltmeters used to measure the probe potential and small drifts in the electrostatic voltmeter reading. As expected, the measured perturbations of the space potential exceed the values predicted by a theory that ignores space charge. Measurements at significantly greater distances above the aperture were prevented by possible contact between the space potential probe and a portion of the top plate which extends downward along the perimeter (fig. 1).

Table 1 Space Potential Perturbations

| Height Above Bottom Plate | %Perturbation of $\Phi'$ [eq(8)] | %Perturbation Measured ($\rho \neq 0$) |
|---|---|---|
| 4R | 0.16 | 0.37, 0.31, 0.48, 0.37 (±0.10) |
| 3R | 0.37 | 0.70, 0.68 (±0.15) |
| 2R | 1.16 | 1.86, 1.60, 1.83, 1.80 (±0.20) |
| 1.1R | 5.96 | 7.05, 6.28 (±0.4) |

The additional perturbation due to air motion was examined by drawing air through the aperture. The air flow was measured with a turbine-type flowmeter and the air speed in the plane of the aperture was calculated by assuming a uniform velocity across the opening. No measureable (i.e. >0.1%) change in space potential could be observed at a height of 11.3 cm (4R) above the aperture for average air speeds between 1.6 m/s to 6.6 m/s in the plane of the aperture.

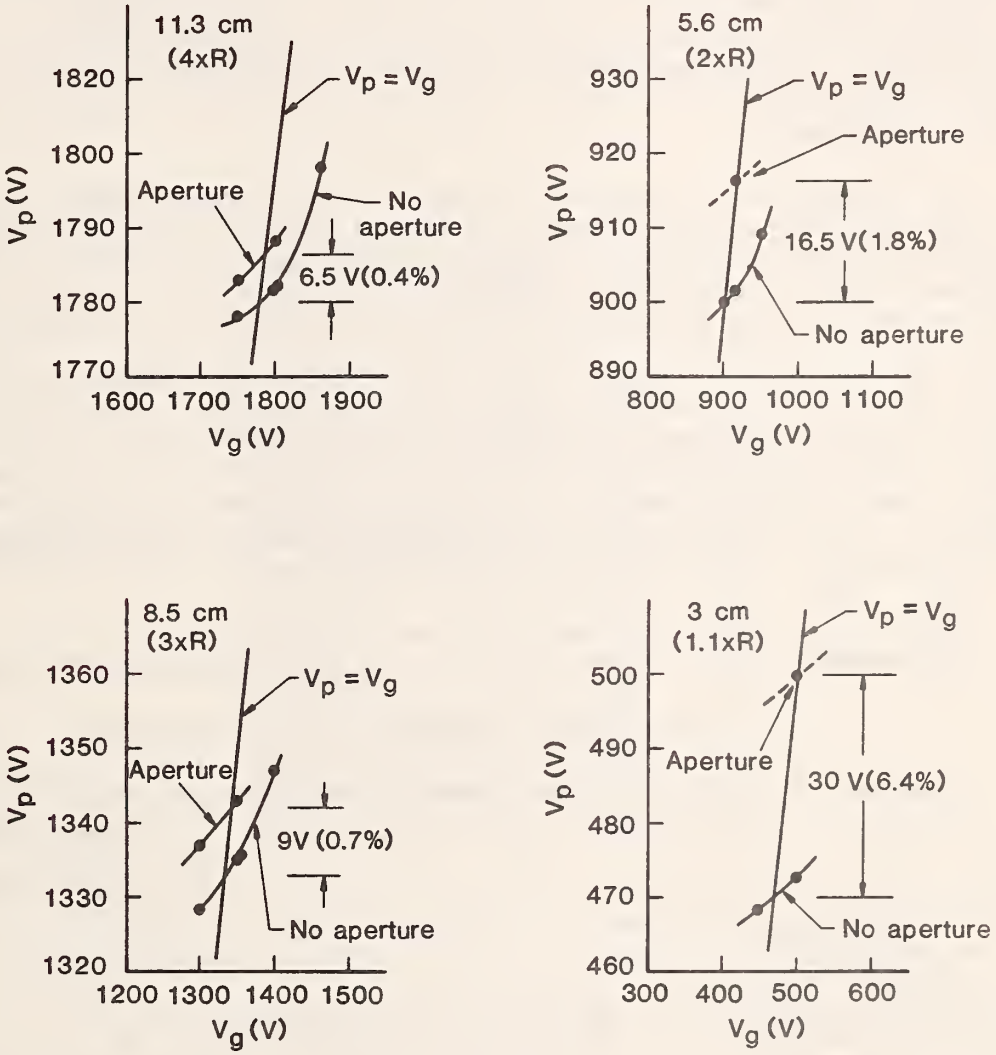


Figure 12. Measurements of space potential perturbation due to 5 cm x 5 cm aperture in ground plane as a function of height above ground plane.

### 6.3 Discussion of Results

The measurements of the preceeding section (for $V_t$=2650 V, $K=1.3 \times 10^{-4}$ $m^2/Vs$, d=0.17 m, $J=0.25 \times 10^{-6}$ $A/m^2$) indicate that the space potential perturbation due to the aperture at a distance of four radii above the aperture is about 0.4%. If the electric field perturbation at four radii above the aperture is estimated using eq (10), a perturbation of less than -1% is expected. The perturbation of E will be smaller yet at the top plate which is 0.17 (6R) above the aperture. For points off the z-axis, the perturbation decreases further.

The absence of any change in probe wire potential because of air flow past the wire four radii above the aperture may not indicate an absence in space potential perturbation. Hara and coworkers have shown that for a cylinder of radius 0.1 m in an electric field with conditions comparable to those in the present measurements, the cylinder potential remains unaffected by air motion if the leakage resistance to ground is less than order $10^{13}$ ohms [20]. It is recalled in this regard that the low space potential measurements reported earlier suggested insufficient resistance between the wire probe and ground. Therefore, one must rely in part on the theoretical arguments made earlier that perturbations of the electric field due to air motion for air speeds of 1 m/s in the plane of the aperture will be insignificant (i.e. <0.1%) near the top of the parallel plate system.

## 7. MEASUREMENT RESULTS: COMPARISON OF CALCULATED AND MEASURED ION DENSITY

### 7.1 Calculated and Measured Ion Densities

Experimental and theoretical results have been presented that suggest for the conditions $V_t$=2650 V, $K=1.3 \times 10^{-4}$ $m^2/Vs$, d=0.17 m, $J=0.25 \times 10^{-6}$ $A/m^2$, and a square aperture of side dimension 0.05 m, significant perturbations of the electric field do not extend to the top plate of the parallel plate apparatus. With approximately the same conditions (the value of K increased slightly to near $1.4 \times 10^{-4}$ $m^2/Vs$), measurements of the ion density were made in the ground plane and compared with calculated values of the charge density. A schematic view of the entrance to the ion counter with some nominal dimensions is given in figure 13. The collector plates in the ion counter are recessed about 10 cm below the plane of the 5 cm x 5 cm aperture and are 7 cm wide. The polarizing plates are recessed behind the collecting plates 3.5 cm. The lengths of the collector and polarizing plates are 18 cm and 14 cm respectively and the spacing is 2 cm. A three terminal measurement of the parallel plate capacitance yielded a value of 212 pF. Polytetrafluorethylene (PTFE) is used to fill the space between the plates and ion counter housing and is recessed behind the collecting plates by 6.5 cm. The square aperture at the entrance of the ion counter is approximately centered over the parallel plates as shown with dotted lines in figure 13. The polarizing voltage for all the measurements was 429 V which was adequate for capturing all the small ions for the air flow rates used during the measurements. That is, the critical mobility, $k_c$, in eq (2) varied between $2.16 \times 10^{-7}$ $m^2/Vs$ to

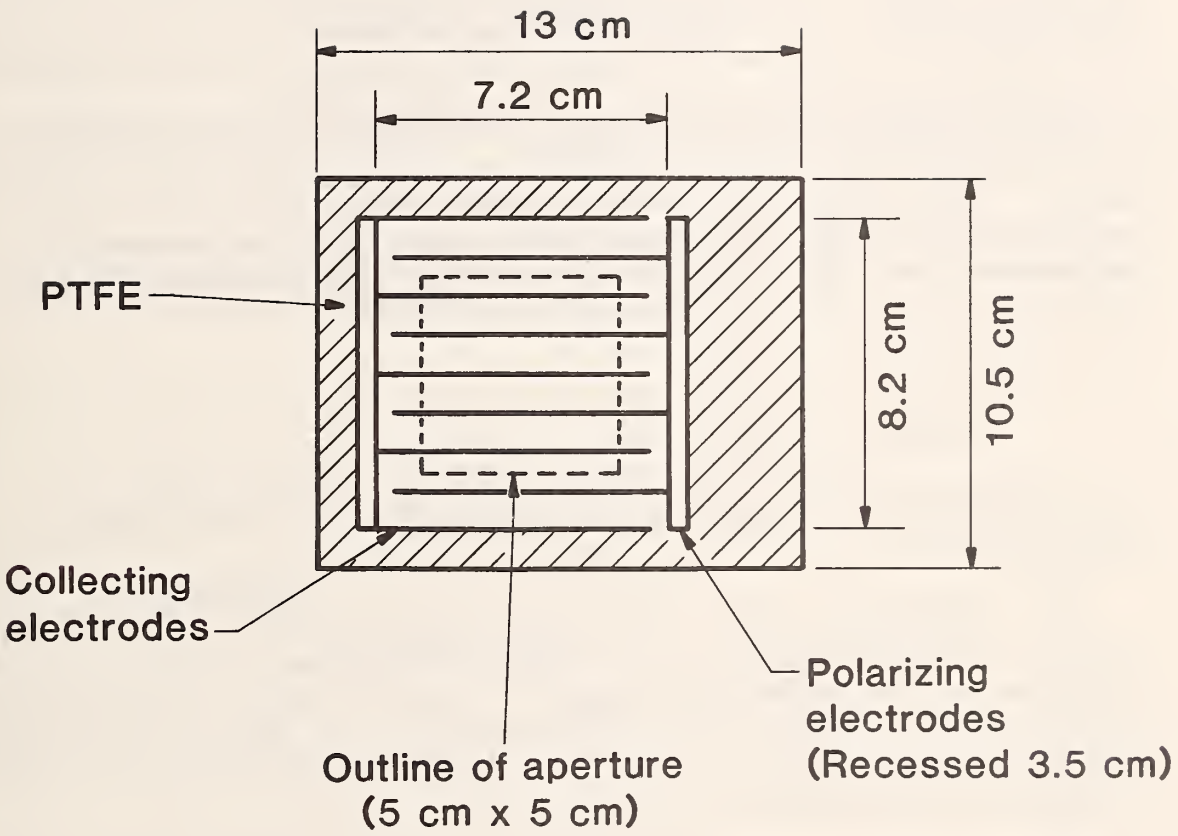


Figure 13. Top view of ion counter entrance with dashed outline of aperture located 10 cm above entrance. Nominal dimensions are indicated. The spacing between the collecting and polarizing electrodes is 2 cm.

$1.58 \times 10^{-6}$ $m^2/Vs$ as the flow rate was increased from $2.22 \times 10^{-3}$ $m^3/s$ to $16.2 \times 10^{-3}$ $m^3/s$. A pump was used to draw air through the ion counter and the air flow was measured with a turbine-type flowmeter. The air flow through the ion counter could be changed by varying the amount of ambient air which was leaked into the pump.

Figure 14 shows the results of positive charge density measurements, $\rho_m$, as a function of average air velocity in the plane of the aperture, assuming a constant velocity across the aperture. Also shown are calculated values of the charge density, $\rho_c$, which are determined using eq (43) and assuming values for $y_o$ and $z_o$ of 13.75 cm and 17 cm respectively. Comparisons of measured and calculated charge density values with the introduction of a 5 cm x 5 cm metal duct extending 5 cm below the plane of the aperture are shown in figure 15.

The uncertainty in calculating $\rho_c$ is estimated by considering the uncertainties in the terms of eq (43). The uncertainty in K is less than ±6% [4]. The uncertainty in J is less than ±6% and takes into account the variation in J on the bottom plate, time averaging of the current measurements, uncertainty of the area of the current sensing patch, and calibration of the electrometer used for the current measurement. $E_o$ is determined from the expression [4]

$$3JV_t/K\varepsilon_o = (E_o^2 + 2Jd/K\varepsilon_o)^{1.5} - E_o^3 \quad , \tag{44}$$

and is dependent on the uncertainties in J and K. The uncertainty in d is less than 0.5%.

The influence of these uncertainties on the value of $\rho_c$ is considered in two parts, (1) the effect on the integral in the numerator in eq (43) and (2) the effect on the factor multiplying the integral (J/K); the integral in the denominator is a constant. The uncertainties in the values of the parameters under the integral sign, for a given $y_o$,$z_o$ pair, leads to an uncertainty in the value of the integral of less than 0.6%.

The values of J and K are determined independently and a root-mean-square (rms) summation could be used to find their combined uncertainty in the quotient multiplying the integral. However, because the 0.6% uncertainty in the integral is correlated with J and K, it is arbitrarily added to the uncertainty in J, i.e., 6% + 0.6% = 6.6%.

As indicated above, the values of $y_o$ and $z_o$ are taken to be 13.75 cm and 17 cm respectively. The value of $z_o$ is obtained by considering the decrease in the values of measured space potential perturbations (Table 1) as extrapolated to the top plate of the parallel-plate system. At the top plate, the space potential perturbation appears to be about 0.2% or less. The electric field perturbation is estimated to be (Section 6.3) about 0.4% or less and considered negligible. The added perturbation due to air motion

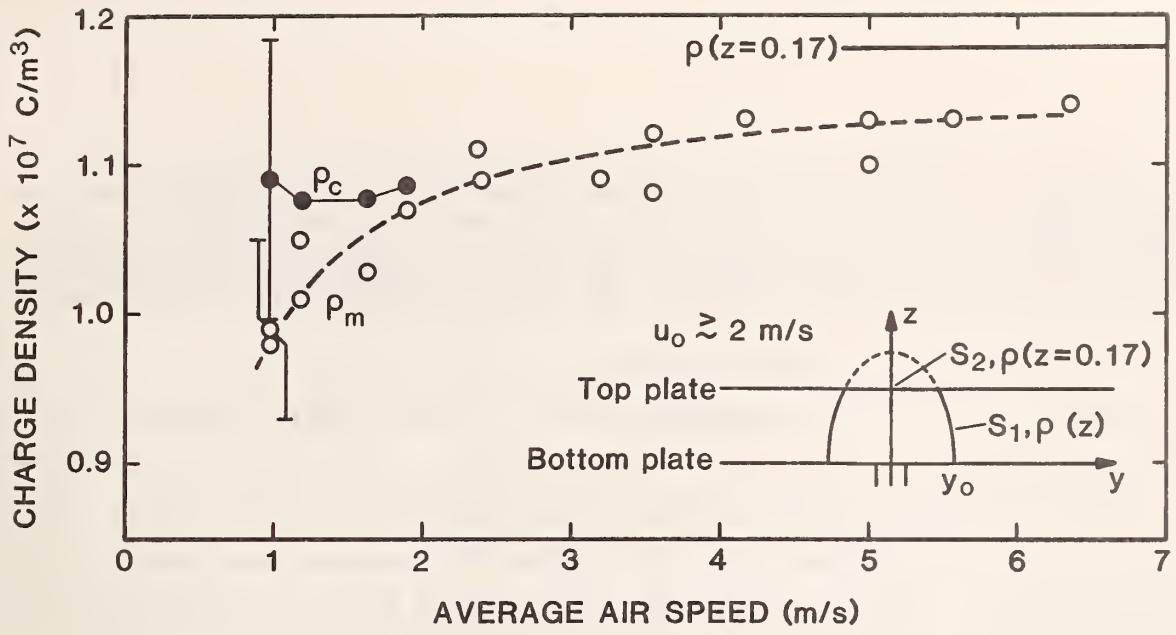


Figure 14. Positive charge density measurements, $\rho_m$, as a function of average air velocity in plane of aperture. Calculated values of the charge density, $\rho_c$, are shown assuming that $y_o$ and $z_o$ are 13.75 cm and 17 cm respectively. Typical error bars are indicated at $u_u$ = 1m/s. As the air speed increases, the surface on which the electric field perturbation remains negligible is represented approximately by a truncated hemi-ellipsoid as shown in inset.

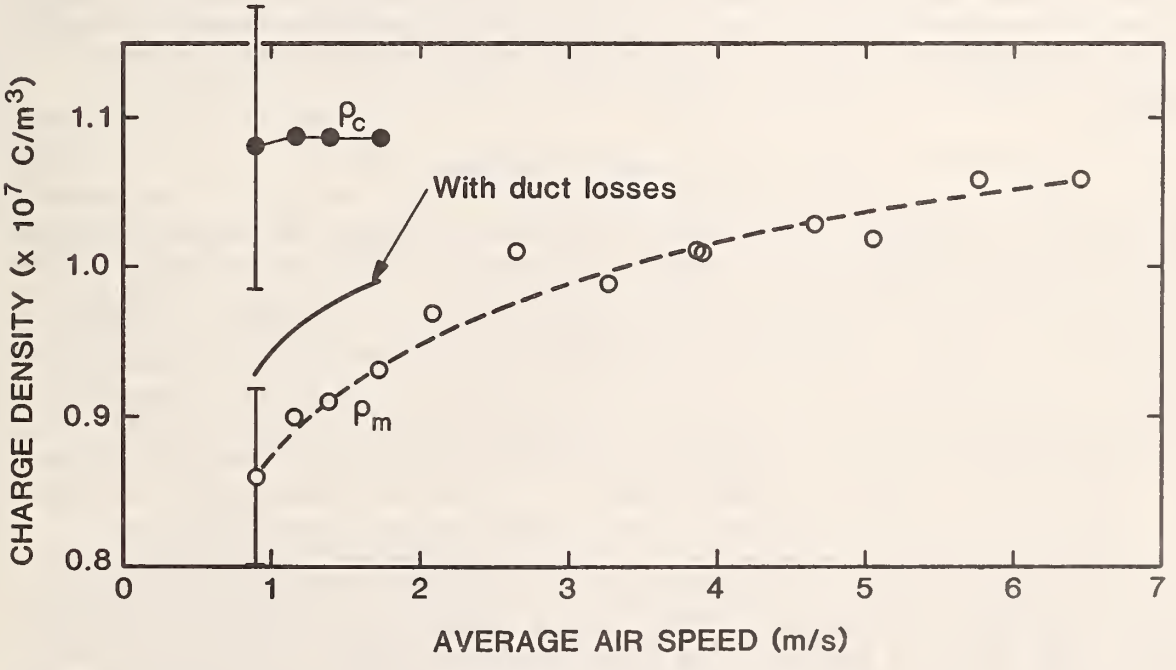


Figure 15. Positive charge density measurements for the same conditions as in figure 14 and with the introduction of a 5 cm long duct below the plane of the aperture. An estimate of ion losses in the duct due to Coulomb repulsion and diffusion, assuming no turbulence, is shown with a solid curve.

through the ion counter for $u_o$ = 1 m/s is also considered negligible. Assuming that the spatial dependence of the electric field perturbation (absolute value) is the same as for the space-charge free case, $y_o$ is 13.75 cm.

The calculated value of charge density, $\rho_c$, is not highly sensitive to the choice of $y_o$ when $y_o$ is so far from the aperture. Allowing an uncertainty of ±3 cm (22%) in the value of $y_o$ leads to less than ±0.9% uncertainty in the value of $\rho_c$. This uncertainty in $y_o$ also takes into account some uncertainty in the distribution of relative air velocities on the surface of integration, $S_o$. The value of $\rho_c$ is not expected to be very dependent on the velocity distributions because, while not isotropic, the distribution of relative air velocities changes slowly on the surfaces that are considered. The total estimated rms uncertainty is therefore taken to be

$$[(6.0\%)^2 + (6.6\%)^2 + (0.9\%)^2]^{1/2}$$

which is less than 9%.

The uncertainty in the values of $\rho_m$ is estimated to be less than ±6%. This figure includes uncertainties in the calibrations of the electrometer used for measuring ion current and the flowmeter for measuring air flow, and statistical fluctuations in the ion current and air flow measurements. The scatter in the measured values of $\rho_m$ indicates the reproducibility of the measurements.

## 7.2 Discussion of Results

The results in figure 14 show that while the measured ion density is less than the calculated charge density when $u_o$ is about 1 m/s, within the uncertainties of the measurement and calculation there is agreement between the values of $\rho_m$ and $\rho_c$. The lower measured value may be due to ion losses in the region between the 5 cm x 5 cm aperture and the 7.2 cm x 8.2 cm opening to the collecting plates (fig. 13) as well as within the ion counter itself. The region between the 5 cm x 5 cm aperture and collecting plates is difficult to model. The airflow is better approximated as a free jet than airflow through a duct. Turbulence at the boundary of the expanding jet occurs [26] and causes mixing with the surrounding air at rest, leading to loss of some ions. Rough calculations of lateral displacement of ions due to Coulomb repulsion and lateral movement of the neutral air, i.e., superposition of displacements, show ion losses that are greater than indicated by the data, which seems unlikely. Thus, while ion losses occur, it may be that the turbulence, in the form of eddy currents of air at the boundary of the jet, prevent the escape of some ions. No attempt was made to theoretically correct the $\rho_c$ values in figure 14 for losses below the 5 cm x 5 cm aperture.

As the air speed through the ion counter is increased, the spatial extent of the electric field (and charge density) perturbation will increase. Assuming for simplicity that the air motion does not greatly change the charge density at the top plate, $\rho(z=0.17\ m)$, an approximate expression for the calculated charge density is given by

$$\rho_c \approx [\int_{S_1} \rho(z)\vec{u}\cdot d\vec{S} + \int_{S_2} \rho(z=0.17)\vec{u}\cdot d\vec{S}]/\int_{S_1+S_2} \vec{u}\cdot d\vec{S}$$

$$\approx [\int_{S_1} \rho(z)\vec{u}\cdot d\vec{S} + \rho(z=0.17)\int_{S_2} \vec{u}\cdot d\vec{S}]/\int_{S_1+S_2} \vec{u}\cdot d\vec{S} \qquad (45)$$

where $S_1$ and $S_2$ are, as shown schematically in figure 14, portions of the boundary surface where the electric field perturbation becomes negligible. As the air speed increases, $S_2$ will increase relative to $S_1$. The contribution of the second term in eq (45) to $\rho_c$ will increase because of the large $\rho$ value ($\rho(z)$ is greatest for z=0.17) and the increasing surface area. The larger values of $\rho_m$ at the higher air speeds likely reflect, in part (duct losses will also decrease), the increased value of the "calculated" charge density.

It is noted that the average air speeds in commercial ion counters are normally less than 1 m/s and the loss of ions in such devices due to Coulomb repulsion and other loss mechanisms could be significant. This is also suggested by the extrapolation of the measured charge density values in figure 14 to air speeds below 1 m/s.

Introducing a square duct that extends 5 cm below the plane of the aperture has a significant impact on the values of $\rho_m$ as shown in figure 15. The solid curve in figure 15 is the calculated density taking into account ion losses due to Coulomb repulsion and diffusion [eqs (35) and (38)] in the duct and assuming no further losses below the duct. An effective radius of 0.0282 m is assumed for the square duct (see Section 6.2 and Appendix B). The solid curve can only be regarded as a rough approximation because of the use of eqs (35) and (38) in a square duct, and because the effects of turbulence, which may be present in the duct for $u_o > 0.6$ m/s, are ignored [27]. As in the case where there is no duct, the ion losses decrease as $u_o$ is increased, reflecting fewer losses in and below the duct, and a larger value of $\rho_c$.

The generally good agreement between calculated and measured values of charge densities in figures 14 and 15 near $u_o$=1 m/s supports Swann's [19] prediction that the extra ions which arrive at the aperture because of the external electric field (compare V′ and V in figures 5 and 6) are lost before reaching the collecting electrodes of the ion counter. The number of extra ions that are lost is significant. The approximate results in figure 5 indicate that when $u_o$ is 1 m/s and E is 15 kV/m, more than twice as many ions could arrive at the aperture than would when there was no electric field [i.e., (V′/V)>2]. The average electric field strength between the parallel

plates for the ion density measurements shown in figures 14 and 15 is near 15.6 kV/m.

It was noted in Section 4 that any electric field lines terminating on the collecting plates of the ion counter could contribute to an excessively high measurement of ion density. The error from this effect will increase if $u_o$ is decreased or if the external electric field, E, is increased because of the greater discrepancy between the volumes V' and V in eq (31). Therefore it is desirable to have some length of duct in front of the collecting electrodes of the ion counter to provide shielding against the external field. The appropriate length of duct can be determined experimentally by observing whether significant ion current to the collecting electrodes can be detected in the presence of the electric field (with ions) when there is no air flow, i.e. M=0. However, for the large ion densities in the vicinity of HVDC transmission lines, the effects of Coulomb repulsion can cause significant loss of ions to the duct. The additional loss due to diffusion may be comparable in magnitude [eq (40)]. Correction for these losses using eq (34) and (39) cannot be readily made, in general, because $\rho_c$, K and the influence of turbulence are not known. There may be some advantage in placing an aperture at the entrance of the duct which is smaller in cross-sectional area than the duct. The measurement results in figures 14 and 15 show that this step can significantly reduce ion losses to the duct. Making $u_o$ as large as practically possible also reduces ion losses. It is cautioned, however, that adding a duct and aperture to a commercial ion counter could affect the airflow, M, because of an increased load on the fan.

While the above steps can reduce the effects of an external electric field and ion losses to a duct, it appears that an experimental calibration will still be required in order to perform charge density measurements with a known uncertainty. The calibration can be a function of average air speed and ion density because of the possible effects of Coulomb repulsion, turbulence and diffusion.

In closing this section, it is interesting to note the relation between $\rho_c$ and the calculated value of $\rho$ in the ground plane. The latter quantity has been used as the "known" value of the charge density during experimental checks of ion counters [13]. For the parallel plate geometry and electrical conditions during the present study, $\rho_c$ exceeded the charge density in the ground plane by about 5.8%. The difference would be greater if the ion contribution to the electric field strength were larger.

## 8. CHARGE DENSITY MEASUREMENTS BENEATH MONOPOLAR HIGH VOLTAGE LINE

In addition to the studies using the NBS parallel plate apparatus, laboratory measurements of charge densities under a monopolar high voltage line have been performed. While the unperturbed charge densities are not characterized as well as in the parallel plate apparatus, the measurement results support the observations made in earlier sections.

## 8.1 Measurements in Ground Plane

Figure 16 is a schematic view of the experimental arrangement used to generate an electric field and current densities at the ground plane similar to those near a HVDC transmission line. The monopolar line, which was 4 m long and 2 m high was connected to a variable high voltage power supply. A square table 1.2 m on a side and 0.3 m high was erected under the line and served as a local ground plane. The table was covered with aluminum, with a line-to-table spacing of 1.7 m. As indicated, the ion counter described in Section 7.1 was located under the table with an inlet 7.5 cm in diameter located in the ground plane. Other instrumentation included a field mill for measuring the electric field and surface mounted current sensors for determining the vertical current density. These current sensors, located on either side of the ion counter inlet and along with the field mill and ion counter inlet, were colinear with the high voltage line. The experiments were performed in a laboratory in which there was limited temperature and humidity control. During the experiments, the temperature varied from 21-27°C and the relative humidity from 55-70%. It should be noted that the value of electric field and current density could not be independently varied, but were determined (for fixed geometry) by the line operating voltage.

The table shown in figure 16 was constructed with a movable center section so that the field and current densities along the line could be mapped for different operating conditions. This was done to determine the uniformity along the line and to insure that the results were not dependent on precise locations of sensing elements. For the line operating voltages of 28, 36, and 47 kV, the electric field and ion current densities along a 0.7 m distance were uniform to within ±3%, for both positive and negative line voltage. For these operating voltages, the nominal electric field had values of 14.8, 20.8, and 29.8 kV/m respectively. The corresponding vertical current densities were 0.1, 0.21, and 0.43 $\mu A/m^2$. Slightly lower values were observed for negative voltage. In practice, the line voltage was adjusted to give the same electric field at the surface of thor both positive and negative voltages.

For a given line operating condition, the air flow through the ion counter was varied and the charge density determined using eq (1). The flow rates were measured using a turbine flow meter. Polarizing potentials were such that for all flow rates, there was complete collection of small ions. During these measurements, the electric field and current to the sensing elements on either side of the counter inlet were also recorded, and used to calculate the charge density at the surface of the ground plane, $\rho_o$, using eq (5). A mobility of $1.4 \times 10^{-4}$ $m^2/Vs$ was assumed for positive ions and $1.8 \times 10^{-4}$ $m^2/Vs$ for negative ions. The results of measurements of $\rho_m$ with positive ions for two electric field strengths as a function of air flow are shown in figure 17.

Because of the complicated duct geometry, the duct losses due to Coulomb repulsion are estimated using eq (36)

$$\rho/\rho_o = [1 + (\rho_o KL/\varepsilon_o u_o)]^{-1} \qquad (46)$$

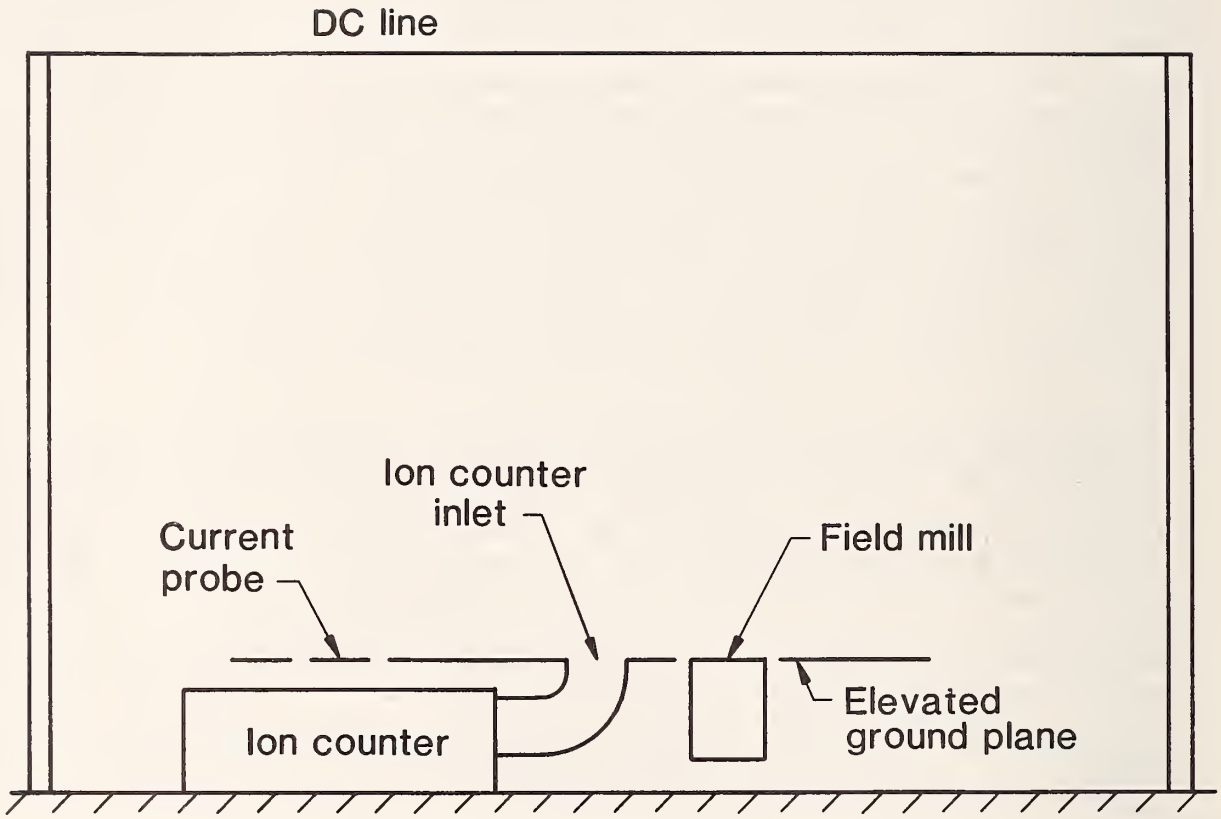


Figure 16. Schematic view of experimental arrangement. Elevated ground plane is located on a table. Relevant dimensions are given in text; figure is not to scale.

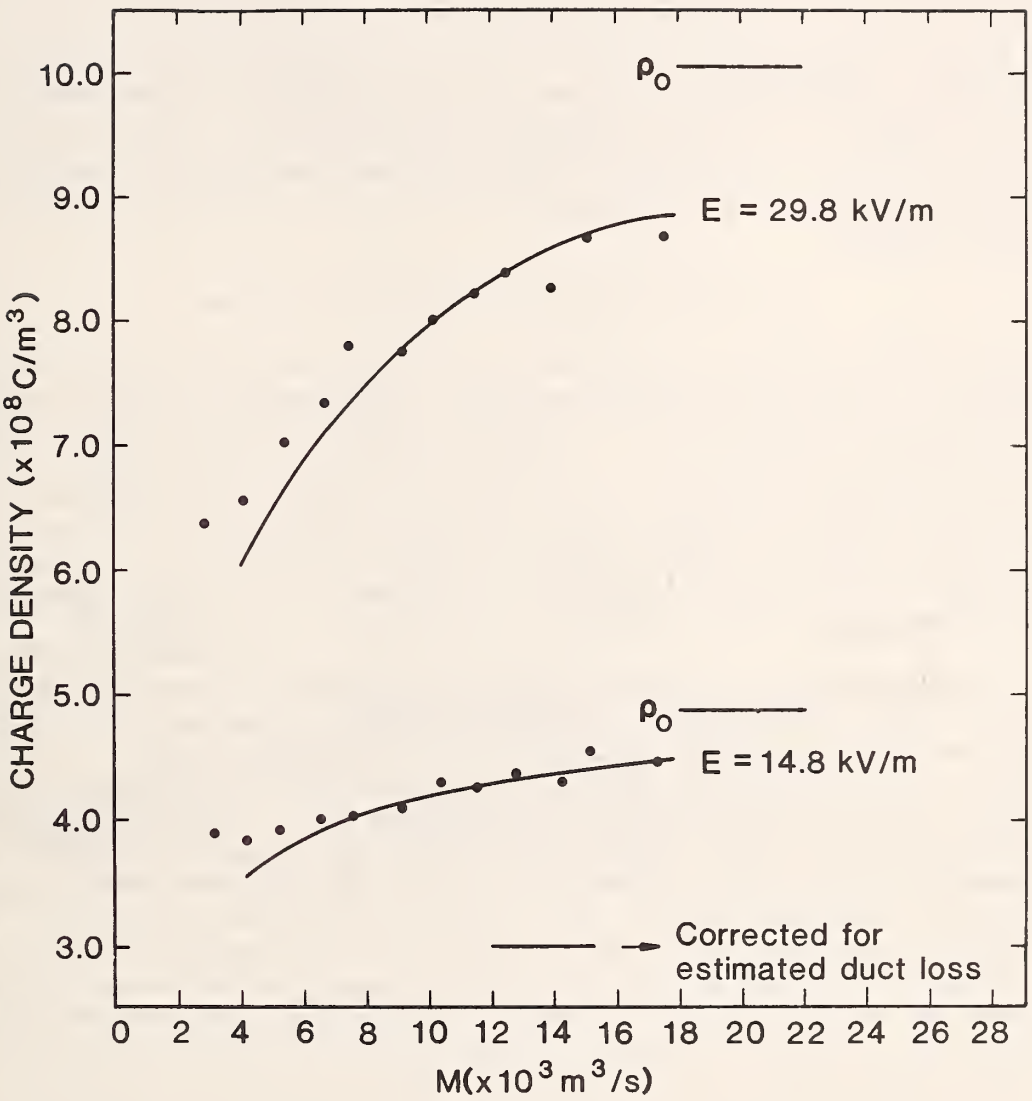


Figure 17. Ion density measurements (solid circles) for different volumetric flow rates M. The ion density values at the surface of the ground plane determined from eq (5) are designated as $\rho_o$. Estimates of duct losses due to Coulomb repulsion are shown as solid curves.

where L is the length of the duct and $u_o$ is the average air speed. Due to the bend in the duct, the calculated values of $\rho$ using eq (46) represent the upper limit on the charge density which can reach the ion counter because of losses due to Coulomb repulsion. The solid curves in figure 17 show the predicted charge densities for two electric field strengths, taking into account duct losses due to Coulomb repulsion using eq (46). The good fit to the data points when M is near 18 x $10^{-3}$ $m^3/s$ is fortuitous because the value of K is assumed and $\rho_o$ instead of $\rho_c$ is used in the calculation. The reasonably good fit of the curves to the remainder of the data indicates that Coulomb repulsion can account for much of the ion losses, and that the charge density measurements appear to be independent of the external electric field as predicted by Swann.

## 8.2 Measurements Above Ground Plane

Ion counters are often operated above the ground plane for reasons of convenience. If the ion counter assembly is referenced to ground potential, ions will either be attracted to or repelled from the ion counter, depending on the polarity of the ions. As noted in Section 6, Swann predicted that the extra ions that are attracted to ion counter because of the external electric field will not reach the collecting electrodes. This prediction was checked by measuring the charge density above the ground plane under a monopolar line; the external electric field near the ion counter was varied by changing the reference potential of the ion counter assembly.

A schematic view of the experimental arrangement is shown in figure 18. The parallel plate ion counter described earlier was raised 0.43 m above the ground plane in a horizontal orientation with insulating supports; the aperture at the entrance was 2.54 cm in diameter and the distance to the collecting electrodes was increased to about 24 cm. A battery operated electrometer, also isolated from ground, was used to measure the ion current. Measurements of the electric field and current density were made in the ground plane using a vibrating plate probe [4] and flat current sensor [6]. Both quantities were uniform within ±10% along the central region of the line. Charge density measurements were made for various line voltages, and one representative set of results is shown in figure 19. The line voltage was -60 kV and the electric field and current density were 27.2 kV/m and 0.63 $\mu A/m^2$ respectively directly under the line. The electric field in the vicinity of the ion counter was controlled by varying the potential of the ion counter with a high voltage dc power supply. Approximate measurements of the unperturbed space potential at heights corresponding to the aperture were performed with an electrostatic voltmeter and radioactively equilibrated antenna [28], and are indicated on the horizontal axis with a cross-hatched area. Charge densities were measured at two flow rates, 4.8 x $10^{-3}$ $m^3/s$ and 15.4 x $10^{-3}$ $m^3/s$. The scatter in the data is due in part to fluctuating air currents in the room which can affect the flow of ions from the monopolar line to the ion counter.

The data again suggests that the measurement is independent of the external electric field for changes in the ion counter potential of approximately 25 kV [29]. Losses begin to occur as the ion counter potential

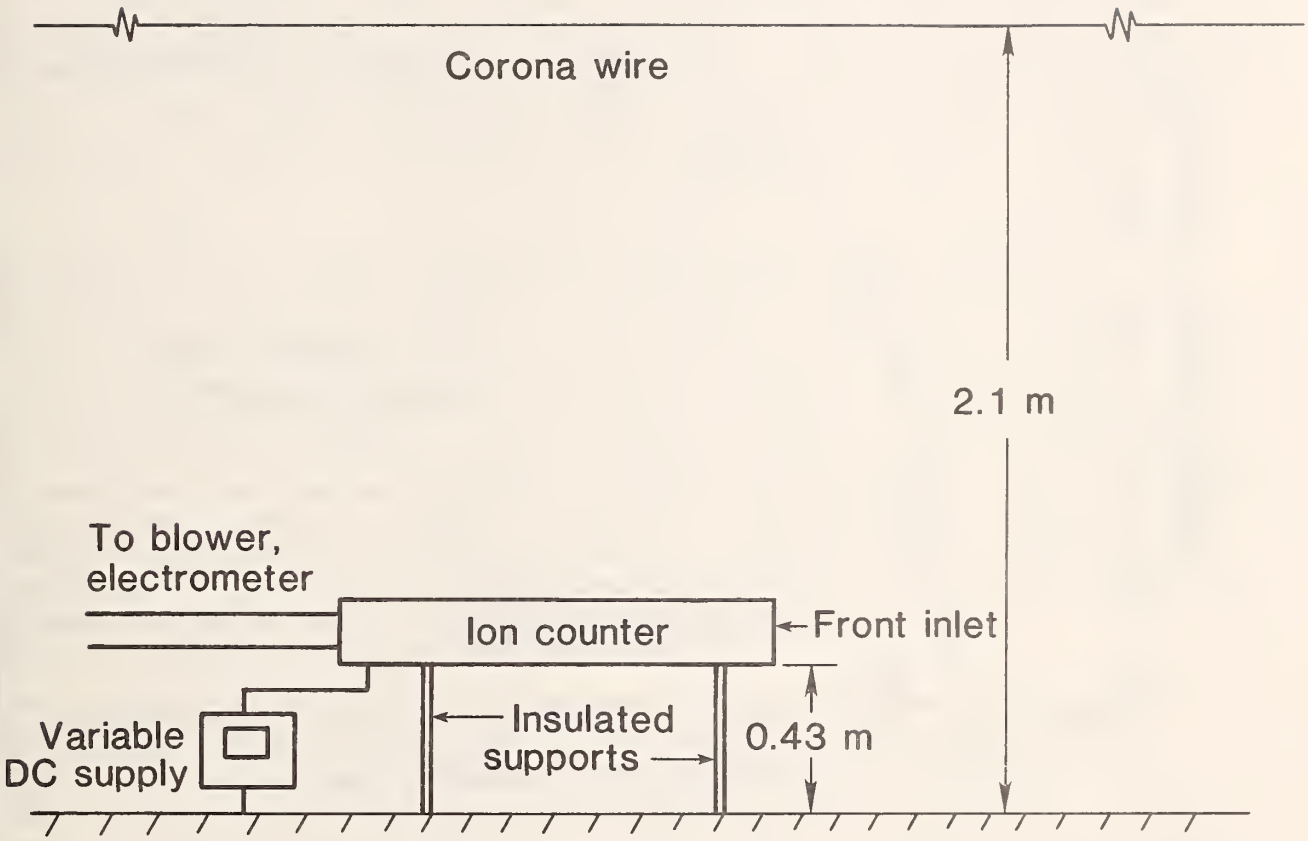


Figure 18. Schematic view of experimental arrangement for above-ground measurements. The polarizing voltage for the ion counter is produced with a battery. Not shown are various measuring instruments, high voltage power supply, etc.

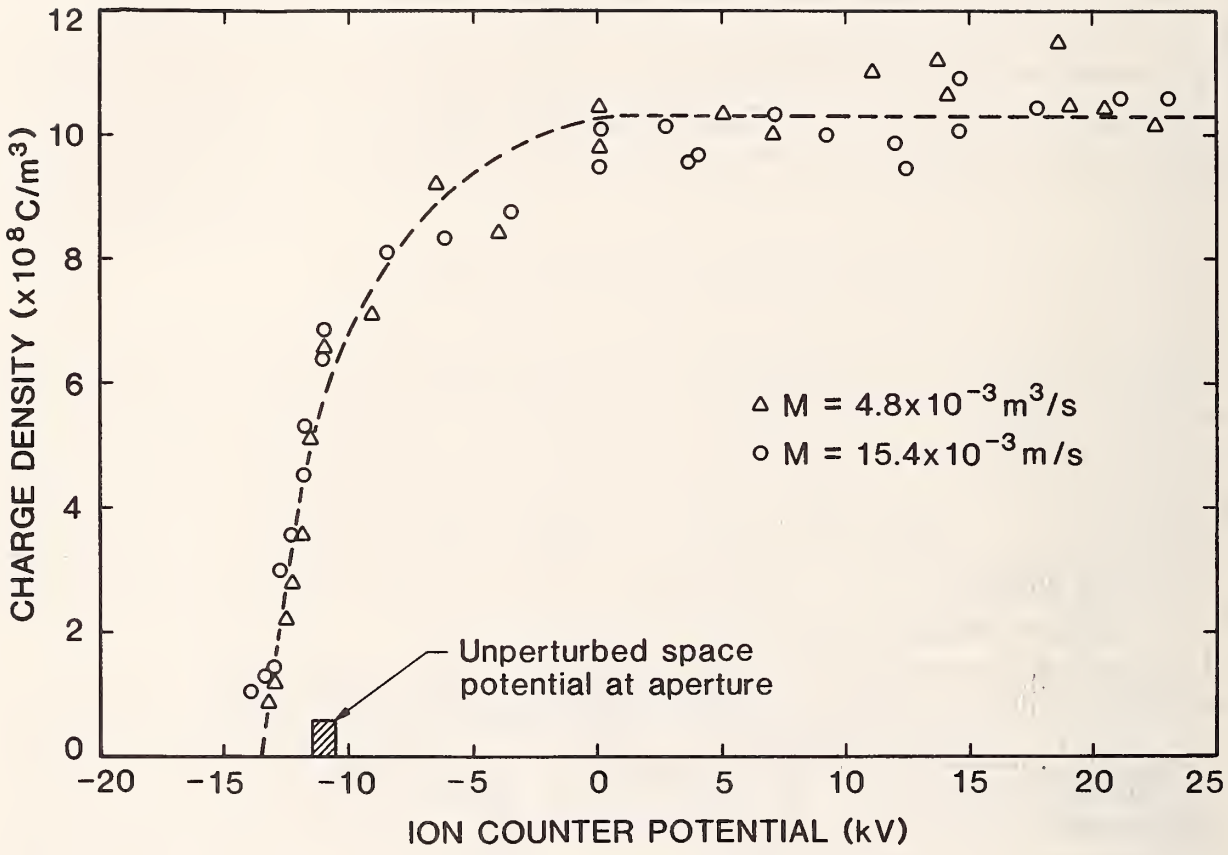


Figure 19. Above-ground ion density measuements at two air flow rates and as a function of ion counter potential. The unperturbed space potential at the height of the aperture, which is 2.54 cm in diameter, is indicated on the horizontal axis.

approaches the unperturbed space potential. At space potential, the ion losses are significant. This result is interesting because the perturbation of the electric field by the ion counter is a minimum at this point.

A qualitative explanation for the loss in ion current is provided in figure 20. Figure 20 shows a schematic view of the ion counter with electric field lines terminating on and leaving the ion counter, when the ion counter is at space potential. Some negative ions with trajectories that approach the ion counter at and from below the height of the aperture will be repelled by the negative induced charges on the ion counter. This repelling action of the induced charges will begin before the ion counter reaches space potential and will increase as the ion counter voltage is made more negative. Swann considered a similar effect when an ion counter was oriented vertically [30].

The above results indicate that the excess ions drawn to the region of the aperture have a small effect on the measurements when they are preferentially attracted to the case of the ion counter and thus grounded through the biasing power supply. If the field configuration is such that the ions are repelled from the vicinity of the aperture, these ions are not counted and significant errors can result. Therefore, the reference potential of the ion counter should be such that charges induced near the aperture by the external electric field attract the ions which are measured. For example, as seen from the results in figure 19, when the ion counter is in a horizontal orientation, a positive reference potential is appropriate. Alternatively, simple electrostatic considerations show that loss of ions can be avoided by operating the ion counter in a vertical orientation and referenced to ground potential. It is recognized, however,that this latter orientation may be more prone to degradation due to contamination.

The effect of an external electric field which enters the opening of an ion counter and reaches the collecting electrodes is considered next. Measurements of ion densities with the NBS ion counter configured so that there is insufficient electrical shielding are shown in figure 21. The ion density measurements were made at three flow rates as a function of reference potential of the ion counter assembly. The experimental arrangement is similar to that shown in figure 18. The small aperture and associated cover plate is removed and allows greater exposure of the collecting electrodes to the external electric field. In this configuration, the opening of the ion counter is 13 cm x 10.5 cm and the collecting electrodes are recessed 10 cm from the opening (see figure 13). No corrections of the data have been made for duct losses, which would make the differences between the different flow rates greater than shown in figure 21. The ion density measurement is now very dependent on the external electric field (i.e., reference potential) and flow rate. For a given flow rate, the measured ion density increases with electric field strength because the volume of ions entering the ion counter (V′ in figures 5 and 6) is increasing relative to the volume of air, V. For a given external electric field (fixed potential on ion counter), the measured ion density increases with decreasing flow rate because the decrease in the volume of air entering the ion counter is greater than the corresponding decrease in the volume of ions.

As noted in Section 7.2, a check for electric field penetration to the collecting electrodes can be made by observing if there is significant ion current to the collecting electrodes when there is no air flow; the ion

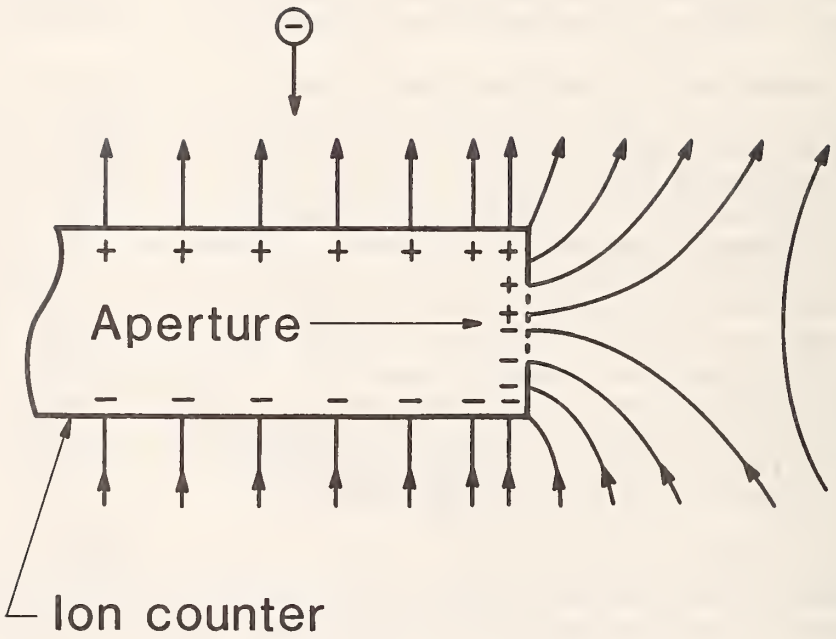


Figure 20. Schematic view of electric field lines terminating on and leaving ion counter near aperture when ion counter is at space potential. The negative charges induced by the electric field repel some negative ions as they approach the aperture under the combined influence of the electric field and air motion.

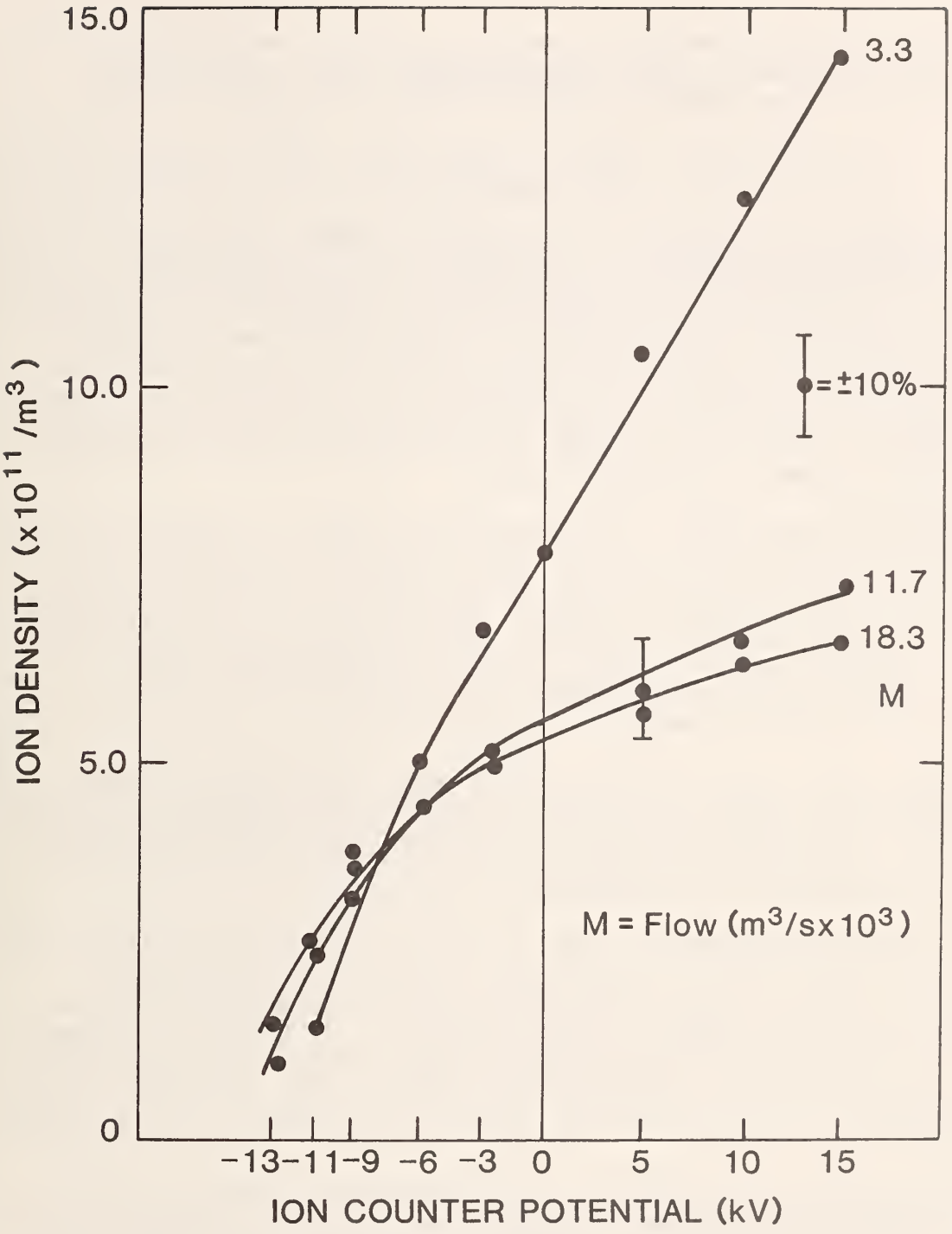


Figure 21. Ion density measurements at different flow rates and as a function of ion counter potential when there is inadequate shielding of the external electric field.

counter, with its large opening, did show such current. When the data in figure 21 are corrected for this "leakage current," the curves develop plateaus for ion counter potentials greater than zero volts.

## 9. SUMMARY

A parallel plate apparatus has been described which is suitable, under certain conditions of voltage ($V_t$), current density and geometry for generating a charge density of known value with an uncertainty of less than ±9%. The acceptability of the apparatus for this purpose was determined theoretically and experimentally by showing that the perturbations of the electric field due to the ion counter aperture in the ground plane and air flow through the aperture did not significantly extend to the top plate of the parallel plates. Thus it was possible to calculate the unperturbed charge density profile between the parallel plates.

Approximate calculations of ion trajectories under the influence of a dc electric field and air motion into the counter show that the number of ions arriving at the aperture is more than when the electric field is absent in agreement with the predictions of Swann. The extra ions are not expected to contribute to the ion density measurement (resulting in a measurement error) unless a significant number of electric field lines terminate on the collecting electrodes of the ion counter, or, equivalently, provided that the excess ions are grounded through the counter's case.

Comparison of calculated charge density values with measured values obtained with an ion counter fabricated at NBS show good agreement within the uncertainties of the calculation and measurements. The use of a duct with a small aperture to minimize the influence of the external electric field as well as duct losses due to Coulomb effects was discussed.

Charge density measurements under a monopolar line provide evidence that an external electric field can significantly influence charge density measurements. The above-ground measurements under a monopolar line showed that operating the ion counter at space potential in a horizontal orientation resulted in ion losses caused by repulsion between the ions and the induced charges on the ion counter. The ion losses can be avoided by biasing the ion counter potential so that ions, of the polarity to be measured, are attracted to the case.

Because there are numerous loss mechanisms for ions entering an ion counter, an experimental calibration would be desirable for characterizing the response of the instrumentation. Unfortunately, because of the large ion densities that are considered for measurements and the associated losses due to Coulomb repulsion, calibration can be a function of ion density. In addition, the calibration is valid only for those conditions in which the only significant air flow is that due to the fan of the ion counter. During outdoor measurements, wind for example, may introduce additional measurement uncertainty.

## 10. ACKNOWLEDGMENTS

The authors are pleased to acknowledge the early contributions of Ralph Kotter to the ion density measurement problem, the assistance of Roberta Cummings during the preparation of the manuscript, and the help of William Anderson and James Hagler during the ion trajectory calculations. Stimulating conversations with A. V. Phelps, W. A. Hoppel, R. V. Anderson and J. C. Willett are also acknowledged. The support of the Electric Energy Systems Division of the Department of Energy made this study possible.

## 11. APPENDIX A: ION LOSSES DUE TO FRINGING ELECTRIC FIELDS FROM ION COUNTERS

As noted in Section 2, significant ion losses can occur due to fringing electric fields from an aspirator-type ion counter. The losses will depend on geometry, polarizing voltage, and volumetric air flow through the system. Results of a simplified model calculation and laboratory measurements are presented here to illustrate the possible magnitude of the problem.

### A.1 Ion Trajectories

An ab-initio analysis of the motion of ions near the ion counter inlet is not possible because of the complicated geometry. However, insight into the loss mechanisms can be gained by using a two-dimensional model and applying numerical analysis methods. A finite element code, resident on NBS computers, has been used to calculate the electric potential distributions and electric field at the inlet of the ion counter. The geometry assumed for the model calculation and the finite element triangulation resulting from the higher level code adaptation of the problem are shown in figure A1. In figure A2, the equipotential values are displayed. A solution was generated for one-half the geometry, since the reflection symmetry inherent in the problem was used to specify the appropriate boundary condition on the midplane. This saves computer space and computation time. An additional simplifying feature involves the assumption that the entrance to the counter is not open, but closed and grounded. Along the boundary intersecting the ion counter electrodes, the potential was assumed to vary linearly between the polarizing and collecting plates.

The calculations are done for a polarizing potential of one unit and the equipotentials are drawn in units of 0.1 of the polarizing potential. For the calculation in figure A2, the polarizing plates are recessed one plate spacing and there is little field leakage. In contrast, figure A3 displays the results of a calculation for a geometry where the polarizing plates protrude one plate spacing in front of the collector plates. Here the extent of the fringing fields is significant. Compare, for example, the location of the 0.1 equipotentials on figures A2 and A3.

While such plots are informative, they do not relate directly to the problem of losses at the inlet. In order to provide quantitative results, a program has been written to calculate the trajectories of ions carried into the ion counter by an air stream. The electric field as calculated using the finite element program and an appropriate air flow velocity field, are stored as arrays. In the program, an ion enters the counter at a particular point. The velocitthat (and any other) point is determined by adding vectorially the air velocity vector and the electrical velocity vector:

$$\vec{v} = \vec{v}_{air} + \vec{v}_E = \vec{v}_{air} + K\vec{E}$$

where K is the ion mobility and $\vec{E}$ is the electric field at the point. Using this velocity, the ion is transported for a predetermined time and, at the new location, the process is repeated. In this way a trajectory for the ion is estimated.

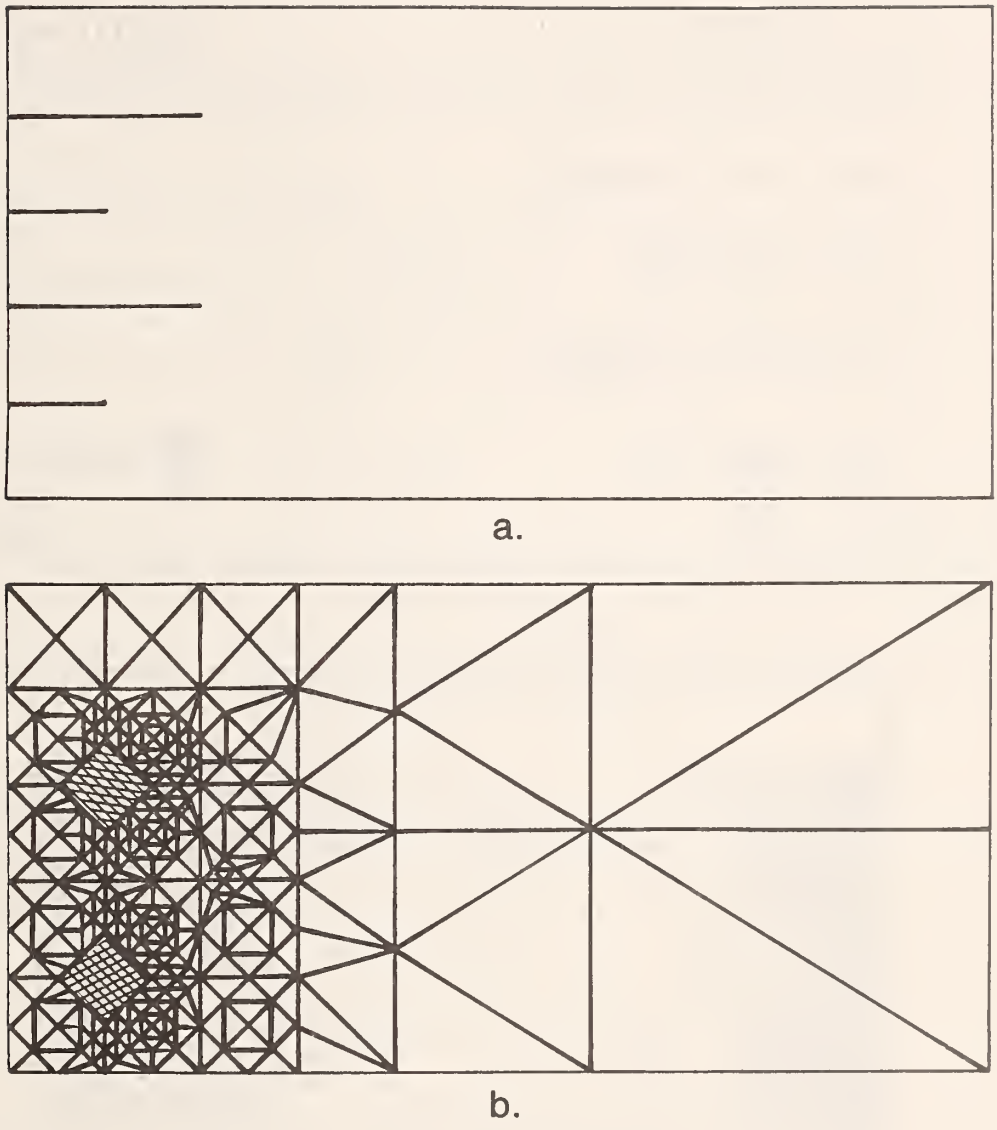


Figure A1. (a) Two dimensional geometry used in finite element calculations. (b) Computer-generated high level triangulation for geometry (a). Inside the cross-hatched area the triangulation was too dense to be displayed.

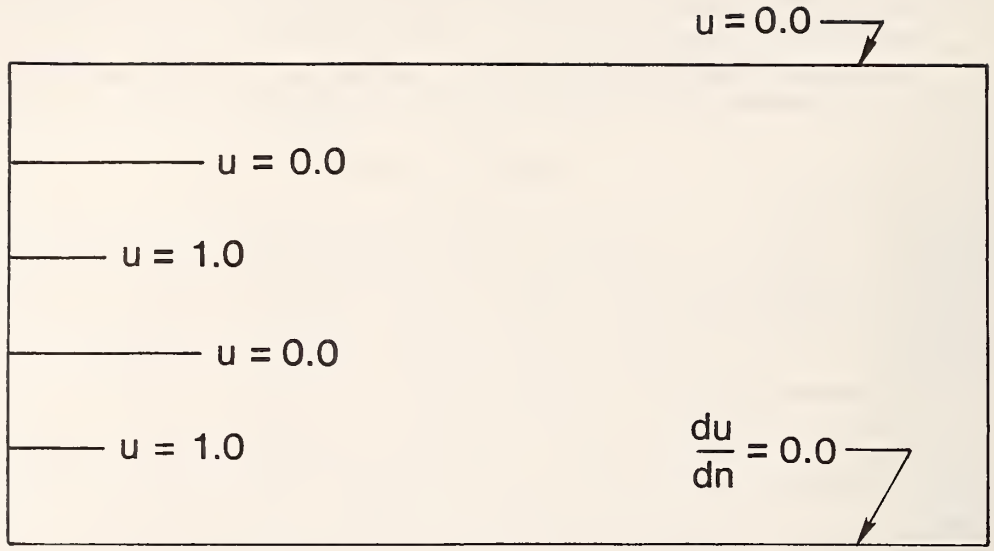


a.

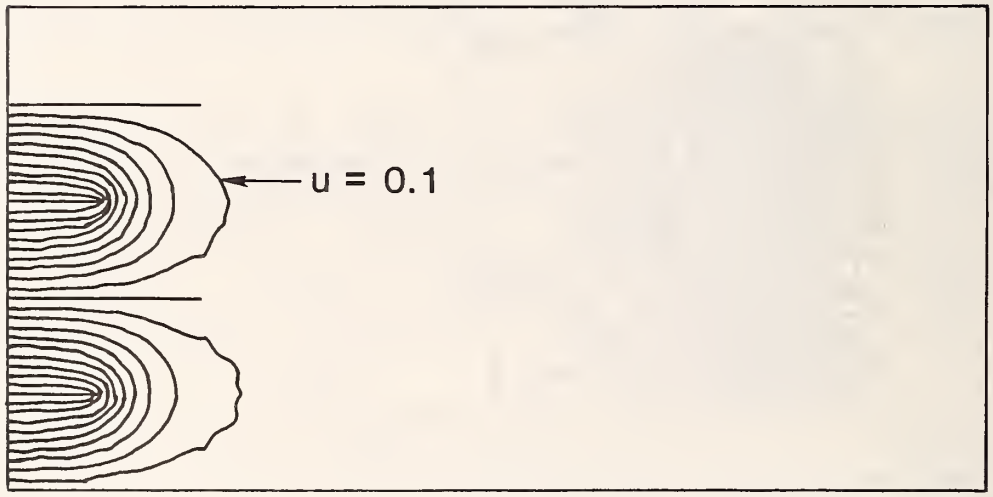


b.

Figure A2. (a) Boundary conditions used in finite element calculation. (b) Computer generated equipotential curves, plotted in units of u = 0.1.

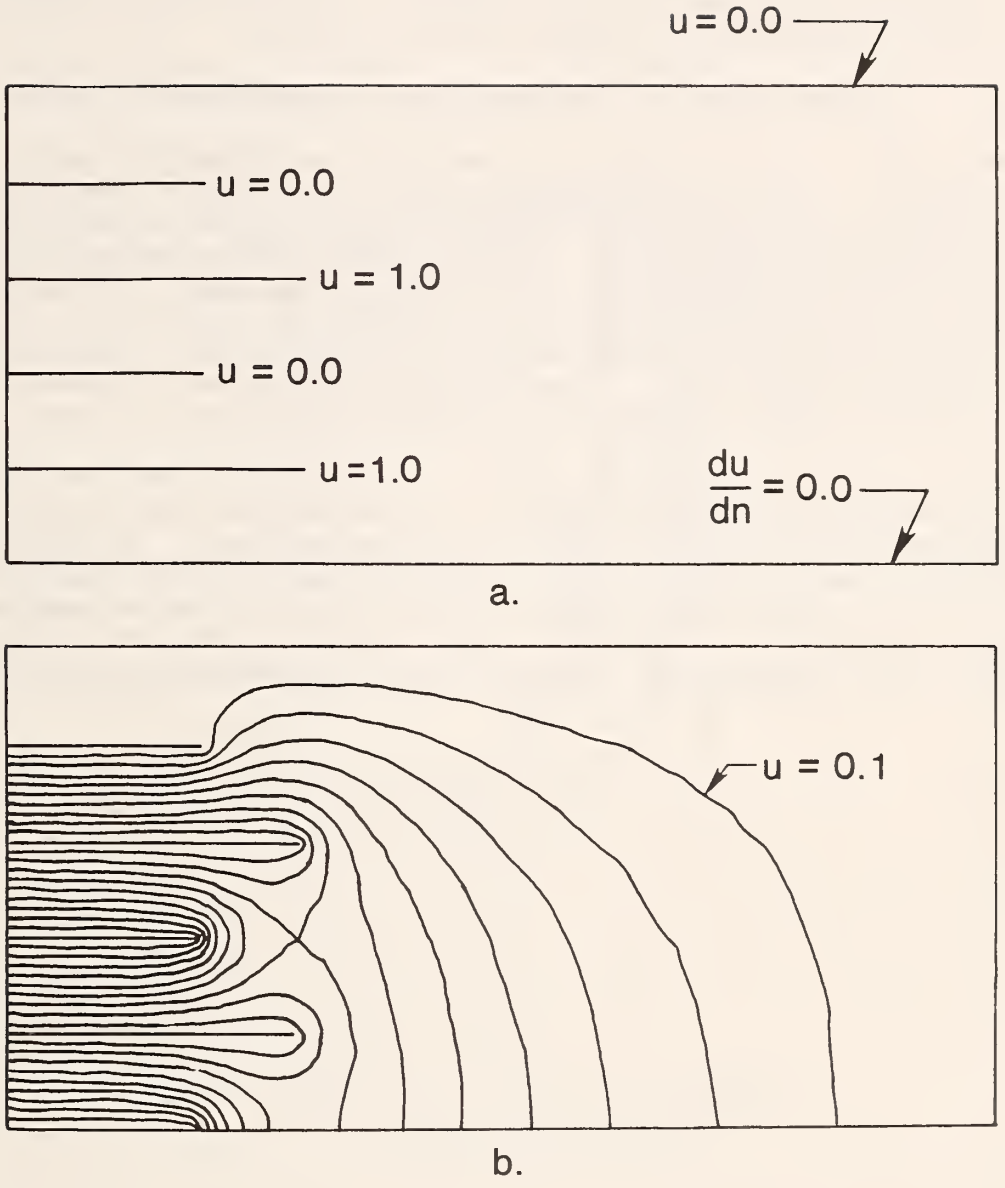


Figure A3. (a) Boundary conditions and geometry used for a model calculation in which the polarizing plates protrude in front of collector plates. (b) Computer generated equipotential curves, plotted in units of u = 0.1.

Sample trajectories for the geometry of figure A3 are shown in figure A4. The ion mobility was taken to be 1.4 $cm^2/V \cdot s$, the polarizing voltage 100 V and the air flow velocity was 42.4 cm/s into the counter.

## A.2 Measurement of Ion Losses and Comparison with Theory

Measurement results showing ion losses due to fringing electric fields are presented in figure A5. Here the relative positions of the collecting and polarizing plates are varied and the positive ion current is measured as a function of polarization voltage. The flow rate and ion density are held constant during the measurements. The air speed averaged over the area of the ion counter entrance was near 42 cm/s. The data show that as the polarizing plates move even with or forward of the collecting plates, there are large losses of ions at the inlet. Losses can occur even when the polarizing plates are recessed one plate spacing (~1 cm) behind the collector plates.

The trajectory calculations (fig. A4) suggest that less than about 25% of the ions reach the collector plates for a polarizing voltage of 100 V whereas the measured loss indicated in figure A5 is not as great. In addition to the simplifying assumptions noted above, the discrepancy between experiment and theory is due in part to assuming an air velocity that has no component orthogonal to the axis of the ion counter. Actually, the streamlines will converge as they approach the entrance of the ion counter (see Section 3.3).

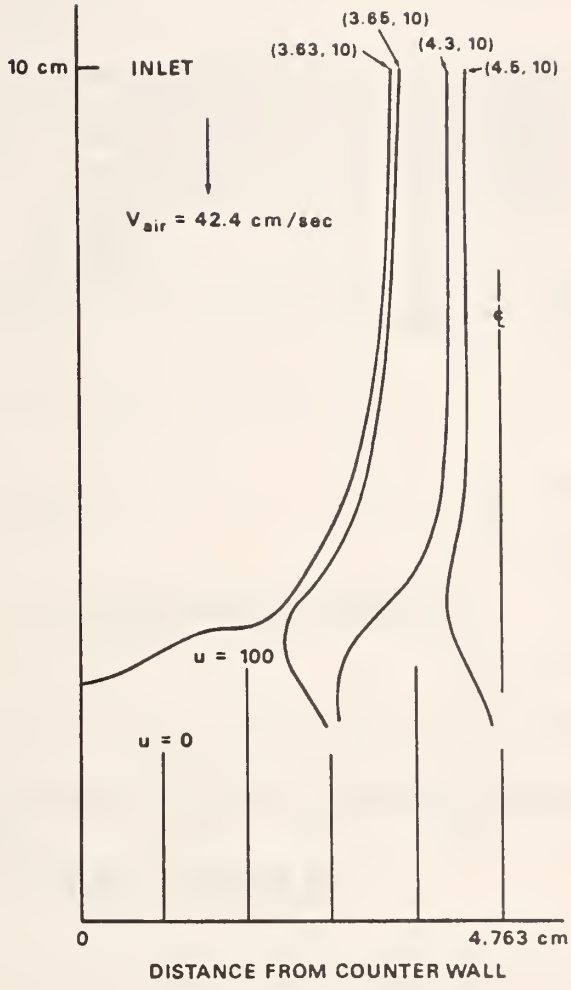


Figure A4. Trajectories of ions entering the ion counter at different initial locations. The geometry is that of figure A3.

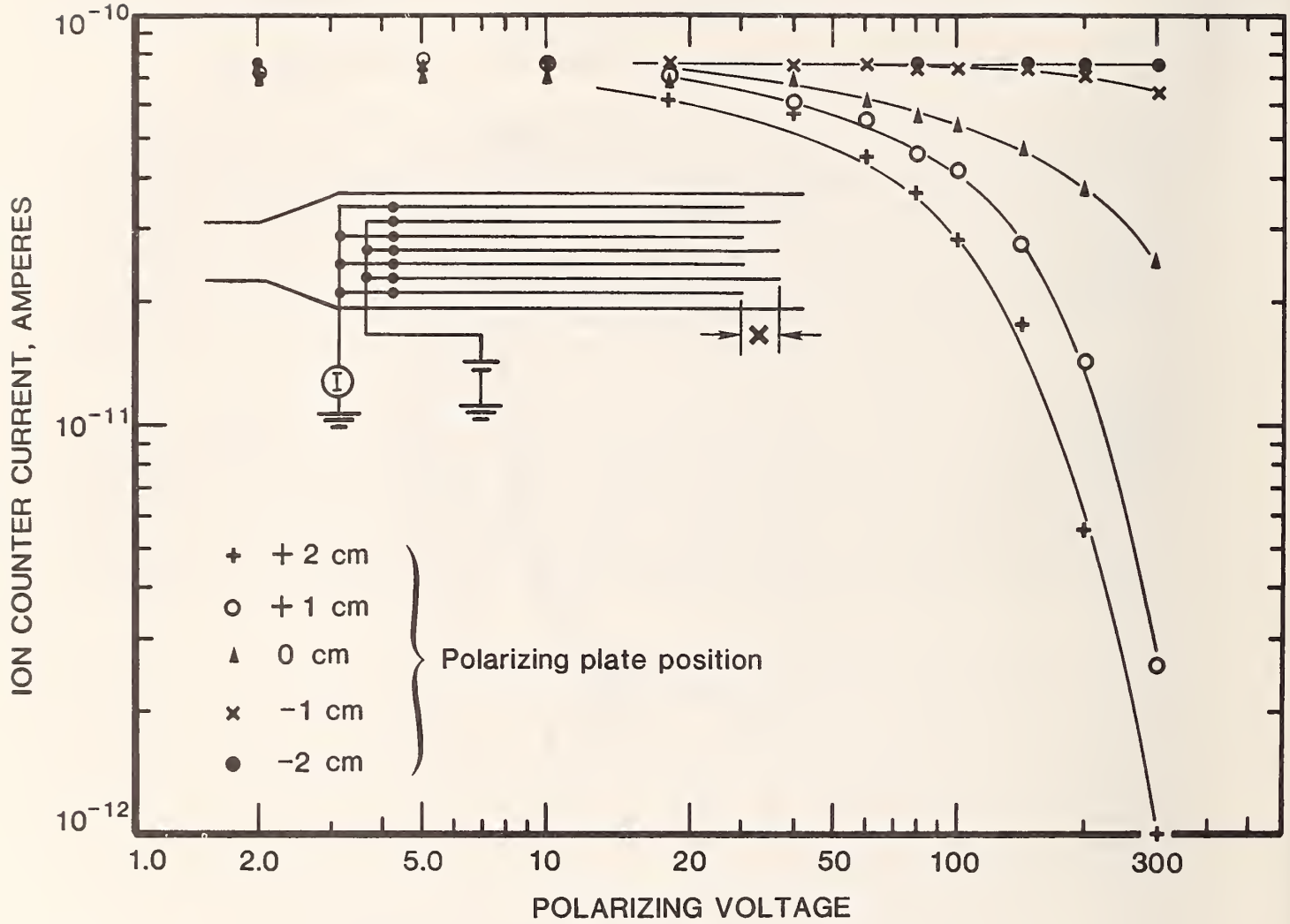


Figure A5. Ion counter output current as a function of polarizing voltage for different plate configurations. The displacement between the leading edges of the collection and polarizing plates is x. Positive values of x correspond to a situation where the polarizing plates protrude in front on the collector plates. For x = 0, the leading edges were flush. Because the ion density is independent of polarizing voltage over the range plotted, the ion counter current should be constant. The spacing of the parallel plates is near 1 cm and the air speed, averaged over the area of the ion counter aperture, is near 42 cm/s.

## 12. APPENDIX B: FLUID FLOW THROUGH AN APERTURE IN A PLANE

An aspirator type ion counter, operated in the ground plane, extracts air from the high field side of the ground plane. This fluid (air) flow can perturb the ion distribution. This perturbation, while it may be less important for measurement near dc transmission lines, may be significant in biological exposure facilities and in laboratory calibration systems.

### B.1 Theory

A distribution of point sinks is used to model the three-dimensional, steady air flow which is induced in a half-space by a known outflow across the boundary. In a rotationally symmetric case, velocities are found analytically. In the general case, numerical integration may be applied to approximate the flow.

Air is drawn into an opening in a broad flat surface at a speed much below that of sound. To determine the flow above the surface, the flow is modeled as steady, irrotational, and incompressible in the upper half-space consisting of points $\vec{r} = (x, y, z)$ such that $z > 0$. We wish to find the velocity, u, satisfying the boundary conditions for $\vec{r}$ in the boundary ($z = 0$):

$$u_n(\vec{r}) = u_o \text{ for } \vec{r} \text{ in } \Omega \tag{B1}$$

$$u_n(\vec{r}) = 0 \text{ for } \vec{r} \text{ not in } \Omega \tag{B2}$$

Here, $u_n$ is the component of $\vec{u}$ normal to the boundary and $\Omega$ is the opening, an open, bounded set of points in the boundary. We also require the velocity at infinity to be zero:

$$\lim_{|\vec{r}|\to\infty} |\vec{u}(\vec{r})| = 0 \quad . \tag{B3}$$

Thus, in the plane $z = 0$, we have the situation shown in figure B1.

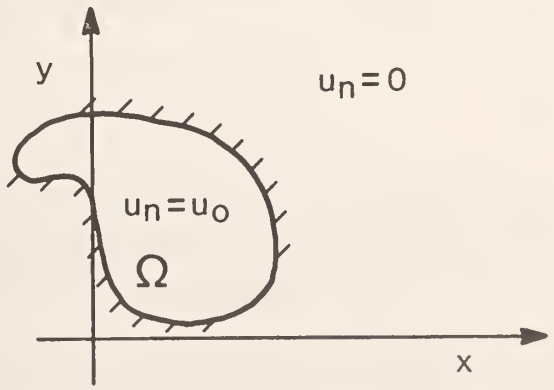


Figure B1. The boundary conditions for flow through aperture of area Ω.

The central idea is to represent the flow field as a linear superposition of point sinks over the region $\Omega$ [17]. It emerges from our analysis that the boundary conditions are satisfied and that for one simple, but important region, $\Omega$, the velocity can be found analytically.

The continuity equation for incompressible flow is

$$\vec{\nabla} \cdot \vec{u} = 0 \quad . \tag{B4}$$

Irrotationality is given by $\vec{\nabla} \times \vec{u} = 0$. The solution for a point sink at $\vec{r}'$ with volume flux m is [31]

$$\vec{u}(\vec{r}) = (-m/4\pi)|\vec{r}-\vec{r}'|^{-3}(\vec{r}-\vec{r}') \quad . \tag{B5}$$

The superposition of point sinks of constant strength which are uniformly distributed over the region $\Omega$, gives rise to the velocity field:

$$\vec{u}(\vec{r}) = (-u_o/2\pi)\int_\Omega\int |\vec{r}-\vec{r}'|^{-3}(\vec{r}-\vec{r}')dx'\ dy' \quad , \tag{B6}$$

where m and $u_o$ are related by $m = 2u_o \cdot$ area ($\Omega$) and m is the volume flux into the sink $\Omega$ from both the upper and lower half spaces. In the case that the flux comes from the upper half only, one must replace the constant

$$(u_o/4\pi) \text{ by } (u_o/2\pi) \quad . \tag{B7}$$

In the interior of the flow, for $\vec{r}$ in the proper half space $z > 0$, the integrand in eq (B6) is absolutely integrable and one may differentiate through the integral to establish that $\vec{u}$ satisfies the differential eq (B4).

Some care must be taken in establishing the boundary conditions, eqs (B1)-(B3). When $\vec{r}$ lies outside $\Omega$ but in the plane $z = 0$, the vector $\vec{r}-\vec{r}'$, which appears in the integrand, has a zero component in the normal direction. The integral converges and so $\vec{u}(\vec{r})$ is defined and has a normal component of zero, i.e.,

$$u_n(\vec{r}) = 0 \quad . \tag{B8}$$

For $\vec{r}$ in $\Omega$, the integrand in eq (B6) has a singularity at $\vec{r}' = \vec{r}$ and is not summable. Consider, however, the velocity at a small distance, d, above the point $\vec{r} = (x, y, 0)$. At $\vec{r}_d = (x, y, d)$, the velocity can be estimated and

$$\lim_{d\to o} u_n(\vec{r}_d) = u_o \quad . \tag{B9}$$

To show this, consider a disk centered at $\vec{r}$ and lying entirely in $\Omega$. Let the disk radius be R as shown in figure B2 and let $r = |\vec{r}'-\vec{r}|$. Integrating separately over the disk and its complement in $\Omega$, and converting to polar coordinates for the disk, one sees that at $r_d$, $d \ll R$, the normal component of the velocity is well estimated by

$$u_n = (u_o/2\pi) \int_o^{2\pi} \int_o^R \frac{d}{(r^2+d^2)^{3/2}} \, rdrd\theta \qquad (B10)$$

$$= u_o \{1- \frac{d}{(R^2+d^2)^{1/2}}\} \quad . \qquad (B11)$$

As $d \to 0$, we get $u_n \to u_o$, which was to be shown.

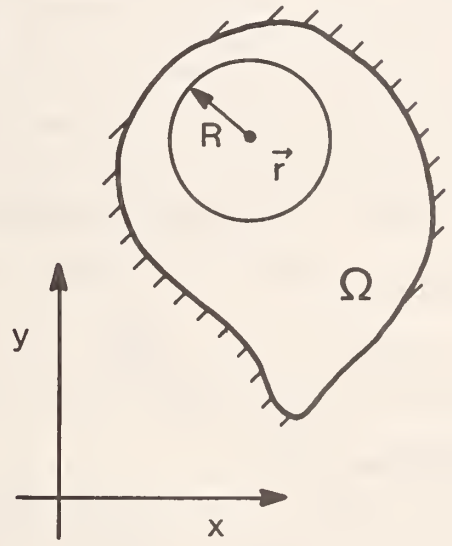


Figure B2. Estimating $u_n$ near $\Omega$.

Note that when $\Omega$ is a disk, the velocity along the central axis, $x = y = 0$, is given by eq (B11). Thus, for a circular hole,

$$\vec{u}(0,0,z) = (0,0,u_o(1-\alpha(1+\alpha^2)^{-1/2})), \quad \alpha = z/R \quad . \qquad (B13)$$

The validity of this model has been verified with measurements made along the central axis (see below).. For a more complicated $\Omega$, the evaluation of $\vec{u}(\vec{r})$ may require a quadrature. Geometric complexity is of no difficulty as long as $\Omega$ can be decomposed into triangles and disks. In this case computer software is available for the necessary calculations.

For application of this method to flows in a half space, the velocities away from the boundary are accurately determined. Neglecting viscosity gives good results because there are no upstream boundaries and consequently no sources of vorticity in the far field. The procedure runs into difficulty at the edge of the region $\Omega$ where the velocity given by this method is infinite. This non-physical solution is the result of neglecting the boundary layer. In the apparatus under consideration, the Reynolds number ranges from 5000 to 30000. For such values, a more accurate determination of flow field in the upstream region is possible, because, for slightly viscous flow, a jet issues on the downstream side of the hole. One must characterize the jet and use it to determine the velocity, $u_n$, at the hole. Then eq (B13) may be used to find the upstream flow more accurately.

## B.2 Comparison of Theory With Measurements

The central velocities given by eq (B13) are found to agree with experiment. Measurements of velocities are made along the central axis lying over a 5.1 cm x 5.1 cm opening using a hot film anemometer. The data is used to fit the model, eq (B13), for a circular opening. Table B1 shows the results of experiment and theory. The measurements are made at different flow rates through the same opening and all data are normalized so u(0.5 cm) = 1. Two techniques are used to find an effective R and the corresponding $u_o$. In case 1, two measurements (d, u(d)) yield two simultaneous equations in $u_o$ and R. These are solved iteratively to find the model parameters. In case 2, one selects R so that $\pi R^2$ is equal to the known area of the opening and $u_o$ is chosen so that u(0.5 cm) = 1. Figure B3 displays the measurements and the theoretical curve of case 2.

Table B1. A comparison of theory to experiment for normalized air speed into a small opening (5.1 cm x 5.1 cm), u(0.5 cm) = 1.

| | Measurement | | | Theory | | | |
|---|---|---|---|---|---|---|---|
| | 1(Δ) | 2(o) | 3(□) | Case 1 | | | Case 2 |
| R | | | | 3.19 | 2.98 | 2.91 | 2.88 cm |
| d | | | | Δ | □ | Δ | |
| 0.0** | Not Measured | | | 1.18 | 1.20 | 1.26 | 1.21 |
| 0.5 | 1.0 | 1.0 | 1.0 | 1.00* | 1.00* | 1.04 | 1.00* |
| 1.5 | .68 | .72 | .66 | .68* | .66* | .68* | .65 |
| 3.5 | .29 | .27 | .25 | .31 | .29 | .29* | .27 |
| 5.5 | .13 | .14 | .12 | .16 | .14 | .15 | .14 |
| 7.5 | .08 | .08 | .10 | .09 | .09 | .09 | .08 |

* Agreement is an artifact of data fitting
** No measurements made, theory gives $u_o$.

Uncertainties in the air speed measurements range from 5% for the highest values, to 10% for the lowest values. The position of the probe is known to within ~1 mm. Assuming the model calculation to be correct, a linear error analysis shows that the uncertainty in $u_o$ is <10%.

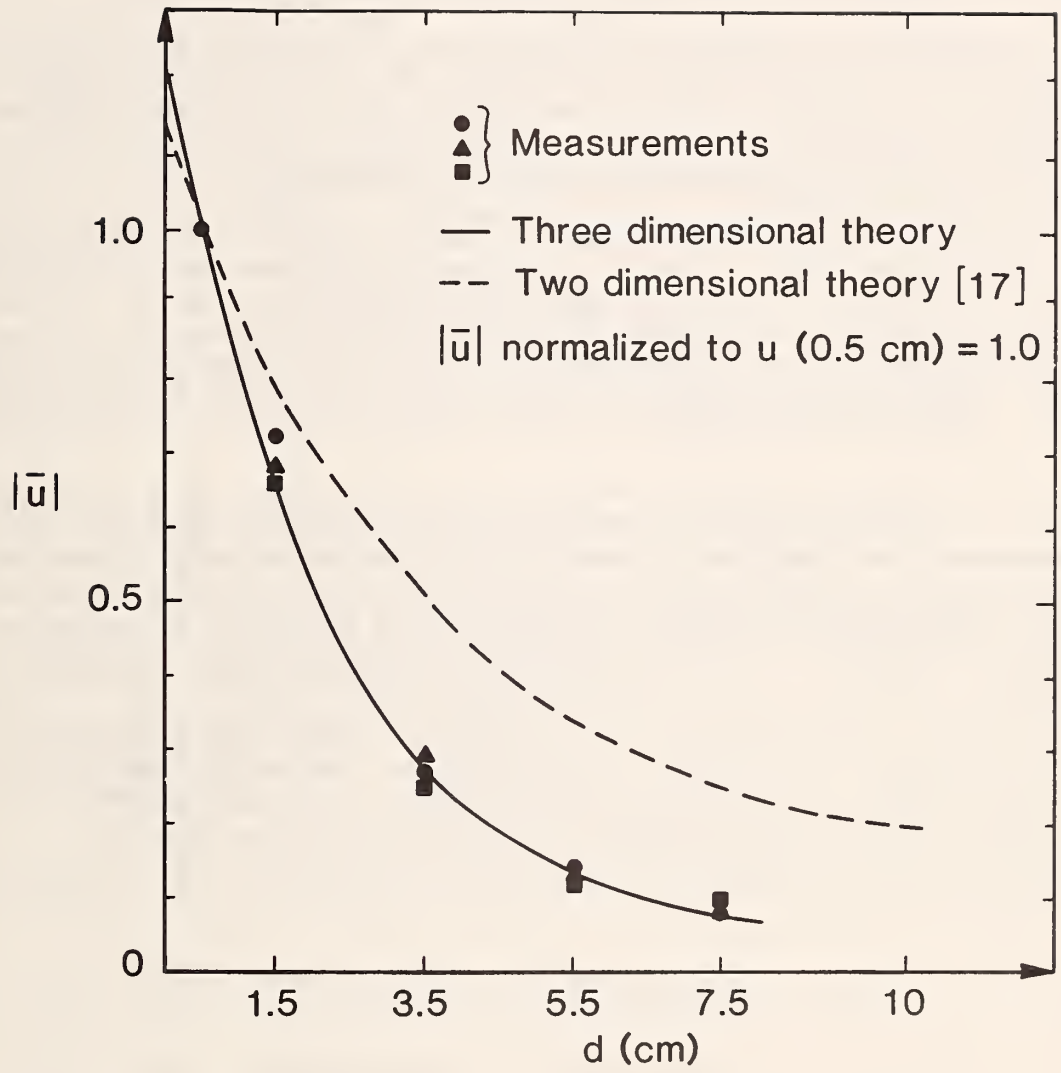


Figure B3. Air speed versus height above a 5.1 cm x 5.1 cm aperture in a plane. The measured values were obtained using three flow rates through the opening, 0.37 x $10^{-2}$ $m^3/s$ (□), 0.69 x $10^{-2}$ $m^3/s$ (o), and 1.7 x $10^{-2}$ $m^3/s$ (Δ). The data have been normalized to unity at d = 0.5 cm.

Equation (B6) can be integrated analytically for a square aperture [see Appendix C, eq (C22)] and yields a more complicated expression for velocity along the z-axis than eq (B13). It is interesting to note that the predictions of eq (B13) using an "effective radius" are in agreement with results obtained using the more rigorously derived expression.

Comparison of theoretical predictions (see eqs (C18) and (C22) in Appendix C) with preliminary measurements of air velocity off the central axis and within a distance of about one diameter from the opening indicate that the predicted values are too high. However, further measurements are required to properly evaluate the theory for off-axis locations.

Attempts to fit the experimental data in figure B3 using the results of a two-dimensional model calculation, a three dimensional model calculation using oblate spheroidal coordinates, and a three dimensional model calculation assuming sinks in the plane of the aperture which increase in strength as the edge of the aperture is approached [17] were less successful than the above model. Results of the two-dimensional theory are shown in figure B3 as a dashed curve for comparison.

In summary, an analytic model of the flow induced by a draft through a hole in a flat boundary has been presented. The model is fully three-dimensional and provides a closed form for the velocity in a problem of interest; i.e., for an aspiration-type ion counter operated in the ground plane. Some work is needed to implement this method on the computer. It is interesting to note that in the evaluation of eq (B6) by quadrature, the boundary condition, eq (B1), can be generalized to allow $u_n(x)$ to vary over the opening. The inclusion of the boundary layer in the model would extend its usefulness to the edge of the half-space, but the influence of this boundary layer at the ground plane is probably not important for the description of the perturbations introduced by the ion counter.

## 13. APPENDIX C: EQUATIONS OF MOTION FOR ION TRAJECTORIES

The equations of motion for ion trajectories under the influence of an electric field perturbed by an aperture in the ground plane and air motion through the aperture are given by eqs (27) and (28)

$$dy/dt = v_y + u_y \quad , \text{ and} \tag{C1}$$

$$dz/dt = v_z + u_z \quad , \tag{C2}$$

where the terms on the right hand side are somewhat lengthy expressions given by eqs (19), (20), (25) and (26). An outline of the derivation of these terms is presented below.

### C1. Ion Drift Velocity

The electric potential between two parallel plates in one of which there is a circular aperture has been determined by Fry and is given by the expression [15]

$$\Phi' = A[\sinh\lambda + (2/\pi) + (2/\pi)\sinh\lambda \tan^{-1}(\sinh\lambda)]\sin\mu \quad , \tag{C3}$$

where A is $E_u R/2$, R is the radius of the aperture, $E_u$ is the unperturbed electric field, and $\lambda$ and $\mu$ are oblate spheroidal coordinates which are related to Cartesian coordinates by the equations

$$\begin{aligned} x &= R\cosh\lambda\cos\mu\cos\theta \qquad 0\le\theta\le 2\pi \\ y &= R\cosh\lambda\cos\mu\sin\theta \qquad 0\le\mu\le\pi/2 \\ z &= R\sinh\lambda\sin\mu \quad . \qquad -\infty\le\lambda\le\infty \quad . \end{aligned} \tag{C4}$$

The equations for the electric field components are derived in the y-z plane ($\theta = \pi/2$) without loss of generality because of the symmetry about the z-axis. Then

$$-E_y = \partial\Phi/\partial y = (\partial\Phi/\partial\lambda)(\partial\lambda/\partial y) + (\partial\Phi/\partial\mu)(\partial\mu/\partial y) \quad , \text{ and} \tag{C5}$$

$$-E_z = \partial\Phi/\partial z = (\partial\Phi/\partial\lambda)(\partial\lambda/\partial z) + (\partial\Phi/\partial\mu)(\partial\mu/\partial z) \quad , \tag{C6}$$

where the prime's have been dropped for simplicity.

The expressions for $\partial\phi/\partial\lambda$ and $\partial\Phi/\partial\mu$ are readily found by differentiating eq (C3). They are

$$\partial\Phi/\partial\lambda = A[\cosh\lambda + (2/\pi)\cosh\lambda\tan^{-1}(\sinh\lambda) + (2/\pi)\tanh\lambda]\sin\mu \quad , \tag{C7}$$

and

$$\partial\Phi/\partial\mu = A[\sinh\lambda + (2/\pi) + (2/\pi)\sinh\lambda\tan^{-1}(\sinh\lambda)]\cos\mu \quad . \tag{C8}$$

To find $\partial\lambda/\partial y$, $\partial\mu/\partial y$, $\partial\lambda/\partial z$ and $\partial\mu/\partial z$, we note from the chain rule that

$$\partial\Phi/\partial\lambda = (\partial\Phi/\partial y)(\partial y/\partial\lambda) + (\partial\Phi/\partial z)(\partial z/\partial\lambda) \quad , \text{ and} \tag{C9}$$

$$\partial\Phi/\partial\mu = (\partial\Phi/\partial y)(\partial y/\partial\mu) + (\partial\Phi/\partial z)(\partial z/\partial\mu) \quad . \tag{C10}$$

Writing eqs (C9) and (C10) in matrix form

$$\begin{pmatrix} \partial\Phi/\partial\lambda \\ \\ \partial\Phi/\partial\mu \end{pmatrix} = \underbrace{\begin{pmatrix} \partial y/\partial\lambda & \partial z/\partial\lambda \\ \\ \partial y/\partial\mu & \partial z/\partial\mu \end{pmatrix}}_{F} \begin{pmatrix} \partial\Phi/\partial y \\ \\ \partial\Phi/\partial z \end{pmatrix} \quad . \tag{C11}$$

The elements of matrix F are readily found from eqs (C4). That is

$$F = \begin{pmatrix} R\sinh\lambda\cos\mu & R\cosh\lambda\sin\mu \\ \\ -R\cosh\lambda\sin\mu & R\sinh\lambda\cos\mu \end{pmatrix} \quad . \tag{C12}$$

Writing eqs (C5) and (C6) in matrix form,

$$\begin{pmatrix} \partial\Phi/\partial y \\ \\ \partial\Phi/\partial z \end{pmatrix} = \begin{pmatrix} \partial\lambda/\partial y & \partial\mu/\partial y \\ \\ \partial\lambda/\partial z & \partial\mu/\partial z \end{pmatrix} \begin{pmatrix} \partial\Phi/\partial\lambda \\ \\ \partial\Phi/\partial\mu \end{pmatrix} \quad , \tag{C13}$$

and comparing with eq (C11), it is seen that the 2 x 2 matrix in eq (C13) is just $F^{-1}$. The inverse of F is readily found from F and is given by

$$F^{-1} = \begin{pmatrix} R\sinh\lambda\cos\mu & -R\cosh\lambda\sin\mu \\ \\ R\cosh\lambda\sin\mu & R\sinh\lambda\cos\mu \end{pmatrix} / D \quad , \tag{C14}$$

where D is equal to $R^2(\cosh^2\lambda - \cos^2\mu)$. The elements of $F^{-1}$ are, from eq (C13), the sought after partial derivatives $\partial\lambda/\partial y$, $\partial\mu/\partial y$, $\partial\lambda/\partial z$ and $\partial\mu/\partial z$. Combining eqs (C7), (C8) and (C14) in eqs (C5) and (C6) and multiplying by the average mobility K gives eqs (19) and (20) for the drift velocities $v_y$ and $v_z$.

## C.2 Air Velocity

The expression for air velocity that is used in calculating ion trajectories is derived in Appendix B and is given by eq (11)

$$\vec{u}(\vec{r}) = -(u_o/2\pi) \iint (\vec{r}-\vec{r}')|\vec{r}-\vec{r}'|^{-3}\, dx'dy' \quad , \tag{C15}$$

where $\vec{r}$ and $\vec{r}'$ are position vectors above and in the plane of the aperture respectively, and x' and y' are Cartesian coordinates in the plane of the aperture. For ion trajectories in the y-z plane,

$$\vec{r} = y\hat{j} + z\hat{k} \quad ,$$

and

$$\vec{r}' = x'\hat{i} + y'\hat{j} \quad .$$

Equation (C15) can thus be written

$$\vec{u}(\vec{r}) = -(u_o/2\pi)\iint(-x'\hat{i} + (y-y')\hat{j} + z\hat{k})(x'^2 + (y-y')^2 + z^2)^{-1.5}dx'dy' \quad . \tag{C16}$$

Equation (C16) can be integrated to yield expressions for the horizontal and vertical velocity components $u_y$ and $u_z$ ($u_x$ is equal to zero) in the y-z plane if a square aperture is considered. To match the edge of the square aperture in the y-z plane with that of a circular aperture, the side dimension of the square aperture is taken to be 2R. The velocity component, $u_y$, is

$$u_y = -(u_o/2\pi) \int_{-R}^{R} \int_{-R}^{R} (y-y')(x'^2 + (y-y')^2 + z^2)^{-1.5}dx'dy' \quad , \tag{C17}$$

which is readily integrated to give

$$u_y = -(u_o/2\pi)\log[(R+F)(-R+G)/(-R+F)(R+G)] \quad , \tag{C18}$$

where

$$F = [R^2 + (y-R)^2 + z^2]^{1/2} \quad , \text{ and}$$

$$G = [R^2 + (y+R)^2 + z^2]^{1/2} \quad .$$

The velocity component, $u_z$, is

$$u_z = -(u_o/2\pi) \int_{-R}^{R} \int_{-R}^{R} z[x'^2 + (y-y')^2 + z^2]^{-1.5}dx'dy' \quad . \tag{C19}$$

Substituting $w' = (y-y')$ and $P^2 = x'^2 + z^2$ leads to

$$u_z = -(u_o z/2\pi) \int_{-R}^{R} dx' \int -(w'^2 + P^2)^{-1.5} dw' \quad , \tag{C20}$$

where P is a constant during integration over w'. Equation (C20) is readily integrated to yield

$$u_z = -(u_o z(y-R)/2\pi) \int_{-R}^{R} (x'^2 + z^2)^{-1} [(y-R)^2 + x'^2 + z^2]^{-0.5} dx'$$

$$+ (u_o z(y+R)/2\pi) \int_{-R}^{R} (x'^2 + z^2)^{-1} [(y+R)^2 + x'^2 + z^2]^{-0.5} dx' \quad . \tag{C21}$$

Both terms in eq (C21) can be integrated using the following expression from a table of integrals

$$\int (ax^2+b)^{-1}(cx^2+d)^{-0.5} dx = [b(ad-bc)]^{-0.5} \tan^{-1}\{x(ad-bc)^{0.5}[b(cx^2+d)]^{-0.5}\},$$

where a, b, c and d are constants that satisfy the inequality ad>bc, After some algebra, $u_z$ can be written

$$u_z = -(u_o/\pi)[\tan^{-1}(R(y+R)/zG) - \tan^{-1}(R(y-R)/zF)] \quad , \tag{C22}$$

where G and F are defined above.

## 14. REFERENCES AND NOTES


[ 1] T. D. Bracken, A. S. Capon, and D. V. Montgomery, Ground Level Electric Fields and Ion Currents on the Celilo-Sylmar ±400 kV DC Intertie During Fair Weather, IEEE Trans. Pow. App. Syst., Vol. PAS-97, pp. 370-378, 1978.

[ 2] M. Hara, N. Hayata, and M. Akazaki, Basic Studies on Ion Flow Electrification Phenomena, J. Electrostatics, Vol. 4, pp. 349-365, 1978.

[ 3] M. Hara, H. Chishaki, and M. Akazaki, Calculation of Electrification Current and Energy Resulting From Ion Flow Under D.C. Transmission Lines, J. Electrostatics, Vol. 6, pp. 29-41, 1979.

[ 4] M. Misakian, Generation and measurement of dc electric fields with space charge, J. Appl. Phys., Vol. 52, pp. 3135-3144, 1981.

[ 5] M. Hara, N. Hayashi, K. Shiotsuki, and M. Akazaki, Influence of Wind and Conductor Potential on Ground Distributions of Electric Field and Ion Current Density at Ground Level in DC High Voltage Line to Plane Geometry, IEEE Trans. Pow. App. Syst., Vol. PAS-101, pp. 803-814, 1982.

[ 6] R. H. McKnight, F. R. Kotter, and M. Misakian, Measurement of Ion Current Density at Ground Level in the Vicinity of High Voltage D.C. Transmission Lines, IEEE Trans. Pow. App. Syst., Vol. PAS-102, pp. 934-941, 1983.

[ 7] P. S. Maruvada, R. D. Dallaire, and R. Pedneault, Development of Field-Mill Instruments for Ground-Level and Above-Ground Electric Field Measurement Under HVDC Transmission Lines, IEEE Trans. Pow. App. Syst., Vol. PAS-102, pp. 738-744, 1983.

[ 8] M. G. Comber, R. Kotter, and R. H. McKnight, Experimental Evaluation of Instruments for Measuring D.C. Transmission Line Electric Fields and Ion Current, IEEE Trans. Pow. App. Syst., Vol. PAS-102, pp. 3549-3557, 1983.

[ 9] H. Israel, Atmospheric Electricity, Vol. 1, translated from second German edition (1970), available from National Technical Information Service, Springfield, VA 22151.

[10] H. F. Tammet, The Aspiration Method For the Determination of Atmospheric-Ion Spectra, translated from Russian (1970), available from National Technical Information Service, Springfield, VA 22151.

[11] H. Ebert, Aspirations apparat zur Bestimmung des Ionengehaltes der Atmosphare, Phys. Z., Vol. 2, pp. 662-666, 1901.

[12] M. Knoll, J. Eichmeier, and R. W. Schon, Properties, Measurement, and Bioclimatic Action of "Small" Multimolecular Atmospheric Ions, in Advances in Electronics and Electron Physics, Vol. 19, pp. 177-254, 1964.

[13] T. D. Bracken and B. C. Furumasu, Field and Ion Current Measurements in Regions of High Charge Density Near Direct Current Transmission Lines,

Proceedings of the Conference on Cloud Physics and Atmospheric Electricity (American Meteorological Society, Boston, 1978) p. 544.

[14] NBS Report NBSIR 83-2761, Development of Power System Measurements--Quarterly Report, January 1 - March 31, 1983.

[15] T. C. Fry, Two Problems In Potential Theory, Am. Math. Monthly, Vol. 39, pp. 199-209, 1932. The solution in this reference does not consider the influence of a connecting tube (ion counter) shown in figure 4. The presence of the tube can be expected to reduce the amount of field perturbation above the aperture.

[16] It is interesting to note that the perturbation along the z-axis of an initially uniform electric field by a conducting spheroidal boss on the ground plane [see P. Moon and D. E. Spencer, Field Theory for Engineers (D. Van Nostrand, 1961), p. 287ff] is also twice that for the electric potential at large z. In the case of a conducting hemisphere, the relative perturbation is exactly two for all points along the z-axis greater than the radius.

[17] H. Lamb, Hydrodynamics (Dover, New York, 1945), p. 98ff, p. 13ff.

[18] A variable step-variable integration algorithm, PLOD, developed at NBS by D. Kahaner was used for the trajectory calculations. See also Guide To Available Mathematics Software, Report No. PB84-171305 (1984), available from National Technical Information Service, Springfield, VA 22151.

[19] W. F. G. Swann, On Certain Matters Relating to The Theory of Atmospheric-Electric Measurements, Terr. Magnet. Atmos. Elect., Vol. 19, pp. 205-218, 1914. Swann's theory does not consider large ion densities for which there is significant Coulomb repulsion between the ions and thus may not be completely valid for the transmission line problem.

[20] Hara et al. have recently shown that the ion current to a cylindrical object in a dc electric field with ions and an air stream is nearly independent of air speed. While fewer ion trajectories terminate on the cylinder at greater air speeds, the ion current to the cylinder remains nearly the same because of the increased ion velocity. See M. Hara, M. Yashima, T. Tsutsumi, and M. Akazaki, Electrification current and voltage on a cylindrical object in the presence of an ion flow field in an air stream, IEE Proc., Vol. 132, Pt. A, pp. 59-66, 1985.

[21] W. T. Kaune, M. Gillis, and R. J. Weigel, Techniques for estimating space-charge densities in systems containing air ions, J. Appl. Phys., Vol. 54, pp. 6267-6273, 1983 and references cited therein. The near equivalence between eqs (35) and (36) can be seen by substituting eq (34) into eq (35).

[22] E. W. McDaniel and E. A. Mason, The Mobility and Diffusion of Ions in Gases (John Wiley, New York 1973), p. 10ff.

[23] Inherent in this model is the assumption that a negligible number of ions fail to reach the aperture because of the zero air velocity at the

surface of the bottom plate. How well J, K, $E_o$ and d can be determined also influences the amount of uncertainty in calculating the known ion density using eq (42) or the approach described in figure 3.

[24] G. W. Penny and R. E. Matick, Potentials in DC Corona Fields, Trans. AIEE, Comm. and Electr., Vol. 79, pp. 91-99, 1960.

[25] R. E. Matick, Potentials in DC Corona Fields, Doctoral Dissertation, Carnegie-Mellon University, 1958.

[26] Profiles of the air velocity across the opening to the collecting plates were obtained with a hot film anemometer. Large fluctuation of the velocity near the boundary of the jet indicated the presence of the turbulence.

[27] While the Reynolds number will exceed 2000 in the duct for $u_o > 0.6$ m/s and it is generally held that turbulence can first occur in tubes when the Reynolds number is between 2000 and 3000, the onset of turbulence may occur at much larger Reynolds numbers depending on conditions in the initial pipe length as well as the approach to it [H. Schlichting, Boundary Layer Theory., Chpt. XVI (McGraw Hill, New York, 1960)]. For example, Cobb reports that turbulence is observed to first occur in a circular tube when the Reynolds number is near 6000 [W. E. Cobb, Ion Losses in the Gerdian Condenser Intake System, J. Appl. Meteorology, Vol. 7, pp. 456-458, 1968].

[28] J. A. Chalmers, Atmospheric Electricity, 2nd ed, (Pergamon, Oxford, 1967), p. 128ff.

[29] Similar results have been observed during conductivity measurements aboard aircraft. See J. H. Kraakevik, The Airborne Measurement of Atmospheric Conductivity, J. Geophys. Res., Vol. 63, pp. 161-169, 1958.

[30] W. F. G. Swann, The Theory of the Action of the Earth's Potential-Gradient In Measurements With The Ebert Ion-Counter, Phys. Rev., Vol. 21, pp. 449-455, 1922.

[31] G. K. Batchelor, An Introduction To Fluid Mechanics (Cambridge University Press, London, 1967), Chpt. II.

☆ U.S. Government Printing Office: 1986—491-070/40083

NBS-114A (REV. 2-8C)

| U.S. DEPT. OF COMM. BIBLIOGRAPHIC DATA SHEET (See instructions) | 1. PUBLICATION OR REPORT NO. NBS/TN- 1223 | 2. Performing Organ. Report No. | 3. Publication Date May 1986 |
|---|---|---|---|

4. TITLE AND SUBTITLE

Calibration of Aspirator-type Ion Counters and Measurement of Unipolar Charge Densities


5. AUTHOR(S)

M. Misakian, R. H. McKnight, C. Fenimore

6. PERFORMING ORGANIZATION (If joint or other than NBS, see instructions)

National Bureau of Standards
Department of Commerce
Gaithersburg, MD 20899


7. Contract/Grant No.

8. Type of Report & Period Covered

Final

9. SPONSORING ORGANIZATION NAME AND COMPLETE ADDRESS (Street, City, State, ZIP)

Same as item 6.

10. SUPPLEMENTARY NOTES

☐ Document describes a computer program; SF-185, FIPS Software Summary, is attached.


11. ABSTRACT (A 200-word or less factual summary of most significant information. If document includes a significant bibliography or literature survey, mention it here)

The characterization of a parallel plate apparatus which can produce a unipolar ion density that is suitable for calibrating aspirator-type ion counters operating in the ground plane is described. The influence of a dc electric field, air motion, Coulomb repulsion and diffusion on the transport of ions into the ion counter are examined to determine their effects on instrument calibration and measurements in the vicinity of high voltage dc transmission lines. An ion density which is known with an uncertainty of less than ±9% is used to check the performance of an ion counter with and without a duct at its entrance. The results of laboratory measurements of ion density under a monopolar high voltage line, which complement the studies with the parallel-plate apparatus, are also described.



12. KEY WORDS (Six to twelve entries; alphabetical order; capitalize only proper names; and separate key words by semicolons)

calibration; instrumentation; ion counter; ion density; measurement; transmission line; unipolar


13. AVAILABILITY

☒ Unlimited

☐ For Official Distribution. Do Not Release to NTIS

☒ Order From Superintendent of Documents, U.S. Government Printing Office, Washington, D.C. 20402.

☐ Order From National Technical Information Service (NTIS), Springfield, VA. 22161

14. NO. OF PRINTED PAGES

74

15. Price

# NBS Technical Publications

## Periodical

**Journal of Research**—The Journal of Research of the National Bureau of Standards reports NBS research and development in those disciplines of the physical and engineering sciences in which the Bureau is active. These include physics, chemistry, engineering, mathematics, and computer sciences. Papers cover a broad range of subjects, with major emphasis on measurement methodology and the basic technology underlying standardization. Also included from time to time are survey articles on topics closely related to the Bureau's technical and scientific programs. Issued six times a year.

## Nonperiodicals

**Monographs**—Major contributions to the technical literature on various subjects related to the Bureau's scientific and technical activities.

**Handbooks**—Recommended codes of engineering and industrial practice (including safety codes) developed in cooperation with interested industries, professional organizations, and regulatory bodies.

**Special Publications**—Include proceedings of conferences sponsored by NBS, NBS annual reports, and other special publications appropriate to this grouping such as wall charts, pocket cards, and bibliographies.

**Applied Mathematics Series**—Mathematical tables, manuals, and studies of special interest to physicists, engineers, chemists, biologists, mathematicians, computer programmers, and others engaged in scientific and technical work.

**National Standard Reference Data Series**—Provides quantitative data on the physical and chemical properties of materials, compiled from the world's literature and critically evaluated. Developed under a worldwide program coordinated by NBS under the authority of the National Standard Data Act (Public Law 90-396). NOTE: The Journal of Physical and Chemical Reference Data (JPCRD) is published quarterly for NBS by the American Chemical Society (ACS) and the American Institute of Physics (AIP). Subscriptions, reprints, and supplements are available from ACS, 1155 Sixteenth St., NW, Washington, DC 20056.

**Building Science Series**—Disseminates technical information developed at the Bureau on building materials, components, systems, and whole structures. The series presents research results, test methods, and performance criteria related to the structural and environmental functions and the durability and safety characteristics of building elements and systems.

**Technical Notes**—Studies or reports which are complete in themselves but restrictive in their treatment of a subject. Analogous to monographs but not so comprehensive in scope or definitive in treatment of the subject area. Often serve as a vehicle for final reports of work performed at NBS under the sponsorship of other government agencies.

**Voluntary Product Standards**—Developed under procedures published by the Department of Commerce in Part 10, Title 15, of the Code of Federal Regulations. The standards establish nationally recognized requirements for products, and provide all concerned interests with a basis for common understanding of the characteristics of the products. NBS administers this program as a supplement to the activities of the private sector standardizing organizations.

**Consumer Information Series**—Practical information, based on NBS research and experience, covering areas of interest to the consumer. Easily understandable language and illustrations provide useful background knowledge for shopping in today's technological marketplace.

*Order the* **above** *NBS publications from: Superintendent of Documents, Government Printing Office, Washington, DC 20402.*

*Order the* **following** *NBS publications—FIPS and NBSIR's—from the National Technical Information Service, Springfield, VA 22161.*

**Federal Information Processing Standards Publications (FIPS PUB)**—Publications in this series collectively constitute the Federal Information Processing Standards Register. The Register serves as the official source of information in the Federal Government regarding standards issued by NBS pursuant to the Federal Property and Administrative Services Act of 1949 as amended, Public Law 89-306 (79 Stat. 1127), and as implemented by Executive Order 11717 (38 FR 12315, dated May 11, 1973) and Part 6 of Title 15 CFR (Code of Federal Regulations).

**NBS Interagency Reports (NBSIR)**—A special series of interim or final reports on work performed by NBS for outside sponsors (both government and non-government). In general, initial distribution is handled by the sponsor; public distribution is by the National Technical Information Service, Springfield, VA 22161, in paper copy or microfiche form.

**U.S. Department of Commerce**
National Bureau of Standards
Gaithersburg, MD 20899